

JPL PUBLICATION 85-66

# Performance Evaluation and Geologic Utility of Landsat-4 Thematic Mapper Data

Earnest D. Paylor  
Michael J. Abrams  
James E. Conel  
Anne B. Kahle  
Harold R. Lang

(NASA-CR-176660) PERFORMANCE EVALUATION AND  
GEOLOGIC UTILITY OF LANDSAT-4 THEMATIC  
MAPPER DATA (Jet Propulsion Lab.) 77 p  
HC A05/MF A01

N86-21970

CSCL 08B

Uncclas

G3/43 05864

October 15, 1985



National Aeronautics and  
Space Administration

Jet Propulsion Laboratory  
California Institute of Technology  
Pasadena, California

JPL PUBLICATION 85-66

# **Performance Evaluation and Geologic Utility of Landsat-4 Thematic Mapper Data**

**Earnest D. Paylor  
Michael J. Abrams  
James E. Conel  
Anne B. Kahle  
Harold R. Lang**

October 15, 1985



National Aeronautics and  
Space Administration

**Jet Propulsion Laboratory  
California Institute of Technology  
Pasadena, California**

The research described in this publication was carried out by the Jet Propulsion Laboratory, California Institute of Technology, under a contract with the National Aeronautics and Space Administration.

Reference herein to any specific commercial product, process, or service by trade name, trademark, manufacturer, or otherwise, does not constitute or imply its endorsement by the United States Government or the Jet Propulsion Laboratory, California Institute of Technology.

## ABSTRACT

This study was part of a continuing program at JPL for the development of remote sensing for geologic applications. The overall objective of the project was to evaluate Landsat-4 Thematic Mapper (TM) data in the context of geologic applications. This involved a quantitative assessment of the data quality including the spatial and spectral characteristics realized by the instrument. Three test sites were selected for the study: 1) Silver Bell, Arizona; 2) Death Valley, California; and, 3) Wind River/Bighorn Basin area, Wyoming. Results of the study demonstrate that the Thematic Mapper sensor is a significant improvement compared to other satellite remote sensing systems. Conclusions of the work include:

- 1) Artificial and natural targets can be used to atmospherically calibrate the TM data and to investigate scanner radiometry, atmospheric parameters, and construction of atmospheric Modulation Transfer Functions (MTF's).
- 2) No significant radiometric degradation occurs in TM data as a result of SCRUNGE processing; however, the data exhibit narrow digital number (DN) distributions suggesting that the configuration of the instrument is not optimal for earth science applications.
- 3) Increased spatial resolution, 1:24,000 enlargement capability, and good geometric fidelity of TM data allow accurate photogeologic/geomorphic mapping, including relative age dating of alluvial fans, measurement of structural and bedding attitudes, and construction of such things as structural cross sections and stratigraphic columns.
- 4) TM bands 5 and 7 are particularly useful for geologic applications because they span a region of the spectrum not previously sampled by multispectral scanner (MSS) data and are important for characterizing clay and carbonate materials. This also allows the separation of iron-bearing and hydroxyl-bearing alteration zones associated with base and precious metal deposits.

## TABLE OF CONTENTS

I.	INTRODUCTION . . . . .	1
II.	OBJECTIVES AND APPROACH . . . . .	3
	A) SILVER BELL, ARIZONA . . . . .	3
	B) DEATH VALLEY, CALIFORNIA . . . . .	4
	C) WIND RIVER/BIGHORN BASIN AREA, WYOMING . . . . .	4
III.	RADIOMETRIC ANALYSIS . . . . .	5
	A) ARTIFICIAL REFLECTANCE TARGET EXPERIMENT . . . . .	5
	B) CALIBRATION OF THE VISIBLE AND NEAR-INFRARED TM DATA .	8
	1) Background . . . . .	8
	2) Method . . . . .	8
	3) Results for Surface Spectral Reflectance . . . . .	9
	4) Determination of Atmospheric Parameters . . . . .	13
	5) Estimates of the Parameter s . . . . .	14
	6) Applications to the Determination of the Atmospheric Modulation Transfer Function (MTF) .	17
	7) Discussion . . . . .	21
	C) DYNAMIC RANGE OF THE TM SYSTEM . . . . .	22
	1) Radiometric Comparison of A-, B-, and P-Format TM Data . . . . .	25
	2) Landsat-4 TM Gains and Offsets: Sensitivity Analysis of TM Radiometry Based Upon Wind River Data . . . . .	25
	3) Sensitivity of TM Radiometry Based Upon Preflight Laboratory Calibration Data . . . . .	27
	D) COMPARISON OF TM AND TM SIMULATOR DATA . . . . .	30
IV.	GEOLOGIC APPLICATIONS . . . . .	33
	A) STRATIGRAPHY . . . . .	33
	B) STRUCTURE . . . . .	41

C)	ALTERATION DETECTION . . . . .	50
D)	LITHOLOGIC MAPPING . . . . .	56
V.	CONCLUSIONS . . . . .	61
VI.	ACKNOWLEDGEMENTS . . . . .	62
VII.	REFERENCES . . . . .	63
VIII.	APPENDIX: PUBLICATIONS AND PRESENTATIONS . . . . .	67

## FIGURES

1.	A representative atmospheric transmission spectrum (after Goetz and Rowan, 1981) . . . . .	2
2.	Artificial target deployment at Lost River, West Virginia test site, October 8, 1982: a) ground photograph looking west; b) NS-001 channel 4 (0.76 to 0.90 $\mu\text{m}$ ) image of target . . . . .	6
3.	Field spectra of target material obtained with the JPL Portable Field Reflectance Spectrometer (PFRS) . . . . .	7
4.	Distribution of image DN vs. surface reflectance for bands 1, 2, 3, 4, 5, and 7 . . . . .	10
5.	Raw DN values of Landsat-4 TM data, Wind River Basin, Wyoming, for selected ground targets . . . . .	11
6.	Calibrated Landsat-4 TM image reflectance spectra for selected sites in the Wind River Basin, Wyoming . . . . .	12
7.	Optical depth as derived from the function $I_2$ . . . . .	15
8.	The phase function $p(\theta)$ determined for the phase angle $\theta = 113^\circ$ and the functions $I_1$ and $I_2$ . . . . .	16
9.	The backscatter function as $\bar{s}$ , determined under assumption of isotropic scattering for the optical depth and single- scattering albedo . . . . .	18
10.	Correlation of the functions $S(\mu, \phi; \mu_0, \phi_0)$ and $\bar{s}$ . . . . .	19
11.	Calibration runs obtained by inclusion of the multiple scattering term $1/(1-R \bar{s})$ in the relationship between scanner radiance DN and surface reflectance R . . . . .	20
12.	Histograms for the Landsat-4 TM image covering the Wind River Basin area, Wyoming . . . . .	23
13.	DN distributions for six Landsat-4 TM scenes . . . . .	24
14.	A gain and offset increase for Landsat-4 TM calculated from calibration results, Wind River Basin area, Wyoming . . . . .	28
15.	The reflectance uncertainty $\Delta R$ at specific wavelengths computed as a function of surface reflectance R . . . . .	29
16.	A full Landsat-4 scene covering a study area in central Wyoming .	34
17.	Same TM image as that shown in Figure 16. The distribution of a redbed stratigraphic marker is highlighted in red . . . . .	35

18.	Landsat-4 TM color composite showing flightlines and 512 x 512 pixel subareas selected for detailed interpretation . . . . .	36
19.	TM bands 2 (blue), 3 (green), and 4 (red) color composite of the Deadman Butte 512 x 512 pixel subarea . . . . .	37
20.	Simplified photogeologic interpretation of a TM image of Deadman Butte area . . . . .	38
21.	True color decorrelation stretch (Soha and Schwartz, 1978) bands 1 (blue), 2 (green), and 3 (red) TM image of the Deadman Butte subarea . . . . .	39
22.	Comparison of a "spectral" stratigraphic column (center panel) measured along flightline 4 (Figures 20 and 21) to TM reflectance profiles (right panel) and conventional stratigraphic column (left panel) . . . . .	40
23.	Stratigraphic correlation from the central Bighorn Basin (Gulf East Lamb well log), through the Deadman Butte subarea (TM reflectance profile, see Figure 22), to the central Casper Arch (Stanolind #1 La Fleiche well log): a) map showing locations of stratigraphic cross-section lines; and b) NW-SE stratigraphic cross section . . . . .	42
24.	Landsat-4 TM bands 2 (blue), 3 (green), and 4 (red) image of the western margin of the Casper Arch showing the outline of the Deadman Butte subarea (Figure 20) . . . . .	43
25.	Stratigraphic panel diagram illustrating a significant, previously unreported increased thickness of the Muddy sandstone facies on the west flank of the Casper Arch . . . . .	44
26.	TM bands 2 (blue), 3 (green), and 4 (red) color composite of the Thermopolis subarea . . . . .	45
27.	Generalized photogeologic interpretation of the Thermopolis subarea . . . . .	47
28.	Correlation of two TM spectral stratigraphic columns . . . . .	48
29.	NE-SW trending TM-derived structural cross sections of the Thermopolis anticline. Each cross section represents a different structural model: a) Drape Fold model (Stearns, 1975); b) Fold-Thrust model (Berg, 1962); and c) Thrust model (Blackstone, 1963) . . . . .	49
30.	TM-derived structural cross section of the Thermopolis Anticline . . . . .	51
31.	TMS data over the Silver Bell copper deposit, Arizona, resampled to 30-m pixels . . . . .	54
32.	Landsat-4 TM data over the Silver Bell copper deposit, Arizona . .	55

33. Geologic map of the Death Valley area from Hunt and Mabey (1966) . . . . .	57
34. Landsat TM principal component image of part of the Death Valley area . . . . .	58
35. Principal component image of the Death Valley area using 13 input variables, including six TM channels, six TIMS channels, and a Seasat Radar image . . . . .	60

#### TABLES

I. Comparison of A-, B-, and P-format calibration parameters of TM data in the Wind River Basin, Wyoming . . . . .	26
II. The quantity $\Delta R'$ computed as the slope of lines in Figure 4 . . . .	31
III. Key to symbols on Figure 32 . . . . .	53

## I. INTRODUCTION

The Landsat-4 Thematic Mapper (TM) sensor is designed to provide increased radiometric, spatial, and geometric performance as compared to the Landsat Multispectral Scanner (MSS). Detailed descriptions of the Landsat-4 satellite and sensor characteristics can be found in Barker and Gunther (1983), NOAA (1983), Salomonson et al. (1980), and Goddard Space Flight Center (1982).

As shown in Figure 1, the TM has six spectral bands in the visible and near infrared (0.4 to 2.5  $\mu\text{m}$ ) and one band in the mid-infrared (10.4 to 12.5  $\mu\text{m}$ ) region of the spectrum. Bands 5 and 7 are particularly useful for geologic applications because they span a spectral region that is important for characterizing geologic surface materials such as clay and carbonate minerals. The system provides 30-m picture elements (pixels) in the visible and near infrared, as compared to 80 m for MSS, and 120-m pixels in the thermal infrared region of the spectrum. Higher radiometric resolution is obtained by recording digital data in 8 bits [256 gray levels or digital numbers (DN's)], instead of 6 bits as with MSS. Thirty-meter pixels permit detection of smaller ground targets; thus, more accurate photogeologic interpretations and determinations of ground locations are possible with TM data compared to MSS data.

This report addresses one part of a continuing program at JPL to advance the state-of-the-art in geologic remote sensing. The overall objective is the evaluation of Landsat-4 TM data for geologic applications. This involves a quantitative assessment of data quality including the spatial and spectral characteristics (photometric and radiometric precision) realized by the instrument.

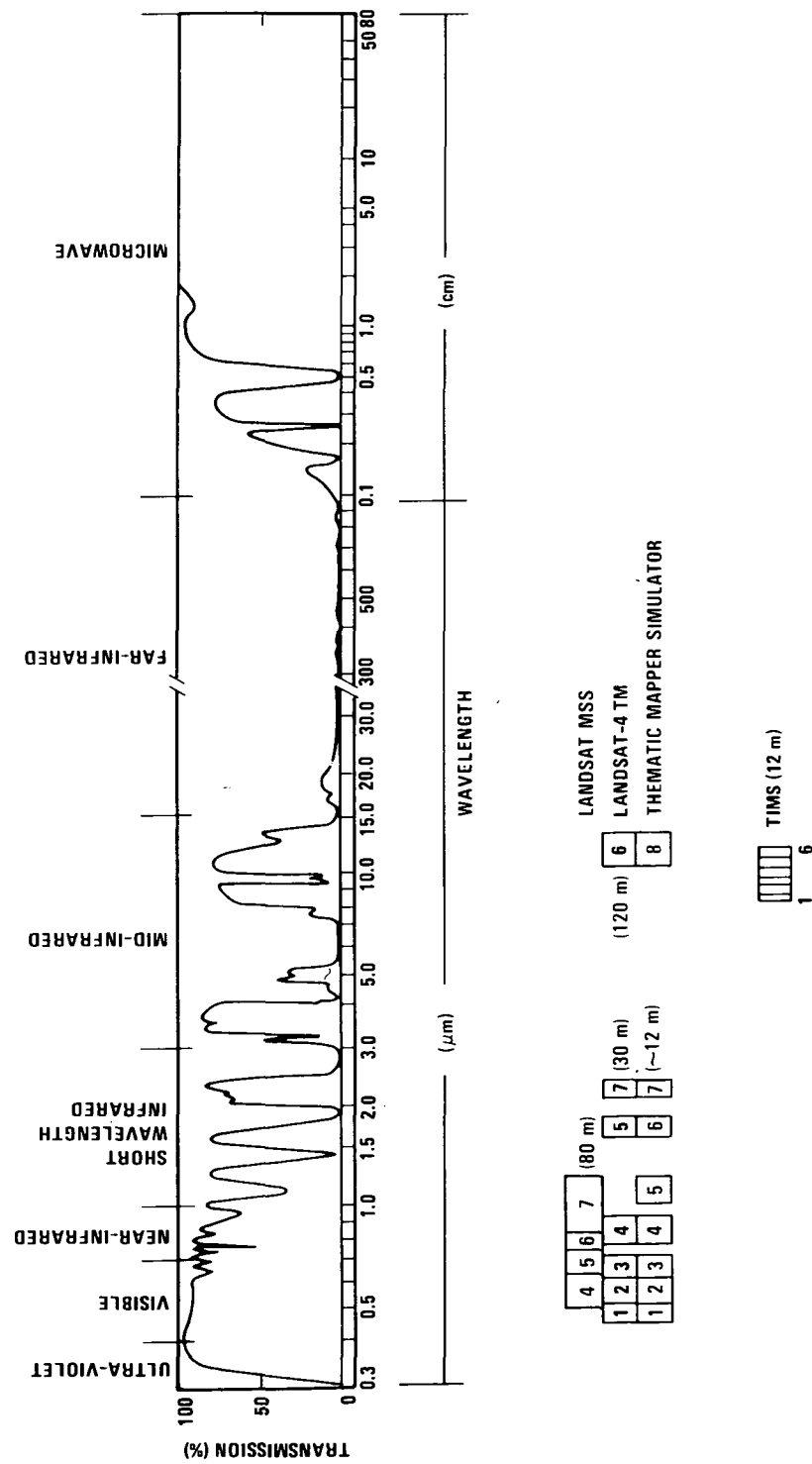


Figure 1. A representative atmospheric transmission spectrum (after Goetz and Rowan, 1981) showing wavelength intervals sampled by selected sensor systems. Picture element (pixel) size is also shown in parenthesis.

## II. OBJECTIVES AND APPROACH

The overall objective of this work was to evaluate Landsat-4 TM data quality in the context of geologic applications. Specific objectives proposed were: 1) to evaluate data quality quantitatively; and, 2) to assess utility for geologic applications. Data quality evaluation included determination of: 1) the effective spatial resolution; 2) the Modulation Transfer Function (MTF); 3) frequency response; 4) edge response; 5) settling time; 6) the calibration of the visible, near-infrared, and thermal bands; and, 7) the geometric registration accuracy of SCRUNGE and TIPS processed data. The assessment of geologic utility encompassed stratigraphic analysis, including lithologic mapping, facies analysis, determination of strike and dip, true stratigraphic thickness, construction of image-defined stratigraphic columns, and stratigraphic correlation, at scales ranging from 1:24,000 to 1:250,000. Structural analysis, including construction of balanced cross sections, at scales of 1:24,000 and 1:250,000 was also assessed, as well as mapping of iron oxide and hydrothermally altered rocks and minerals, and relative age-dating of alluvial fans. Due to the unavailability or poor quality of certain TM scenes because of weather or seasonal problems, we were unable to evaluate some TM characteristics including frequency response, edge response, settling time, effective spatial resolution, and absolute calibration of the thermal channel. Geometric registration accuracy was assessed in the context of geologic applications and is discussed qualitatively in the geologic applications section of this report.

The work was to be conducted in two phases. Phase I, aimed primarily at quantitative evaluation of data quality, was to be initiated as soon as possible after launch of Landsat-4 and conducted at a test site in Lost River, West Virginia. The area was previously studied during the joint NASA/Geosat Test Case Project (Abrams et al., 1985). We proposed to compare TM data to already studied aircraft NS-001 TM Simulator (TMS) data and MSS data to examine the TM performance and its usefulness for geologic and botanical applications. We deployed two large artificial targets (ninety meters square each) at the site at the time of TM data acquisition in order to examine instrument characteristics such as calibration, MTF, edge response, settling time, effective spatial resolution, etc. The targets were successfully deployed. Cloud cover, however, precluded analysis of TM data. Phase I of the project was therefore discontinued and, where possible, phase I tasks were addressed at phase II sites.

In phase II of the project, we acquired and analyzed Landsat-4 TM data over locations which had already been studied extensively using MSS, TMS, and Heat Capacity Mapping Mission (HCMM) satellite thermal data along with field spectral reflectance and thermal measurements. This phase of the project, conducted in the Western U.S., was aimed at determining how well TM data met geologic requirements. The study sites included the NASA/Geosat Porphyry Copper Test Site at Silver Bell, Arizona; the HCMM test site at Death Valley, California; and the Wind River/Bighorn Basin area, Wyoming, which also includes the NASA/Geosat Uranium Test Site at Copper Mountain.

### A) SILVER BELL, ARIZONA

The Silver Bell, Arizona porphyry copper deposit was selected during the NASA/Geosat Test Case Project to study the spectral discriminability of

hydrothermal alteration facies and structural controls related to porphyry copper mineralization. The geologic history of the area has been influenced by a WNW-trending fault zone that served to localize the intrusion of shallow-level stocks and sills into host rocks consisting of limestone, volcanics, and older intrusive rocks. Hydrothermal alteration of the host rocks produced mineral assemblages dominated by the presence of hydroxyl-bearing minerals. TMS data were by far the most useful of the data sets analyzed during the NASA/Geosat study of the area, providing the best separation of alteration facies and rock-type discrimination. Ancillary data assembled for this site facilitate evaluation of new remote sensing tools, in this case the Landsat-4 TM.

#### B) DEATH VALLEY, CALIFORNIA

We have mainly examined thermal remote sensing techniques at Death Valley, California (e.g., Gillespie, 1984; Kahle and Goetz, 1983; Kahle et al., 1984). Located in the Basin and Range structural province, Death Valley is a deep graben which is partially filled with saline lake deposits (sediments) and flanked by large alluvial fans and remnant Tertiary volcanic rocks. Surrounding bedrock units are dolostones, shales, limestones, quartzites and volcanic rocks such as rhyolitic tuffs and basalts. Satellite and registered aircraft scanner data (thermal, visible, and near-infrared) exist for the site at a spatial resolution greater than that provided by the TM, and also at a lower spatial resolution (500-m HCMM). These data have been used, along with site visits and ancillary data, to characterize the surface thermal and reflectance properties of rocks exposed in the area.

#### C) WIND RIVER/BIGHORN BASIN AREA, WYOMING

The Wind River and Bighorn Basins of Wyoming are being studied for the Multispectral Analysis of Sedimentary Basins Project. The basins are Rocky Mountain Foreland sedimentary basins. Well-exposed, structurally deformed sedimentary rocks ranging in age from Cambrian to Recent (excluding Silurian), crop out around the basin margins. Uplifts, cored by Precambrian granitic and metasedimentary rocks, and extrusive igneous rocks surround the basins. An extensive collection of remotely sensed data and a data base of ancillary data are available for comparison with TM data in evaluating their utility for studying the evolution of sedimentary basins.

### III. RADIOMETRIC ANALYSIS

#### A) ARTIFICIAL REFLECTANCE TARGET EXPERIMENT

Experiments were conducted with artificial targets to calibrate, evaluate atmospheric effects, and determine radiometric precision and spatial characteristics of the TM system. Dense cloud cover at the time of TM data acquisition precluded data analysis, but these experiments did demonstrate the feasibility of using plastic calibration targets for such studies.

Black and white target pairs were deployed once at Mountain Pass, California [August 19, 1982, at the time of an NS-001 (TMS) aircraft overflight] and twice at Lost River, West Virginia (October 8 and 24, 1982, at the time of Landsat-4 TM overpass and simultaneous NS-001 overflight). The purpose of the Mountain Pass deployment was to determine the feasibility of the method, and of the two Lost River deployments, to use the method for TM data analysis.

Targets had the following characteristics: a) material -- 6-mil TU TUF polyethylene in 20 ft x 100 ft sheets; b) shape -- square, 25 m x 25 m at Mountain Pass and 90 m x 90 m (3 x 3 TM pixels) at Lost River (see Figure 2); c) orientation -- boundary between target pair was perpendicular to scan direction of sensor systems; and, d) spectral characteristics -- one target of high albedo and one of low albedo in the spectral interval sampled by the scanner systems. Spectra were measured in the laboratory with the Beckman DK2A and UV5240 spectrophotometers before field deployment and also in the field with JPL's Portable Field Reflectance Spectrometer (PFRS) (Figure 3) and Hand Held Ratioing Radiometer (HHRR), and with Gulf's Collins field spectrometer. Target temperatures were also monitored in the field with the Barnes Precision Radiation Thermometer (PRT-5). All field measurements were coincident with scanner data acquisition.

Although cloud cover at the time of Landsat-4 TM data acquisition at Lost River precluded analysis, these experiments did demonstrate:

- 1) TU TUF plastic sheeting is an adequate, spectrally homogeneous target material that can be used as a standard for investigating scanner calibration and radiometry problems;
- 2) large (over 4 acres) artificial targets can be rapidly deployed, spectrally characterized in the field during scanner overpasses, removed, and reused;
- 3) artificial target-derived ground reflection calibration curves were successfully obtained for NS-001 data in the Mountain Pass experiment; and,
- 4) preflight adjustment of offset and gain settings for the NS-001 sensor are possible using sample target material.

Such adjustment is required to insure that the reflectance of the targets deployed in the field falls within the dynamic range of the scanner system. Based upon preflight laboratory calibration data for the Landsat-4 TM system and solar illumination/atmospheric modeling, reflectance of targets used for these experiments falls within the dynamic range of the Landsat-4 TM system.

ORIGINAL PAGE IS  
OF POOR QUALITY.

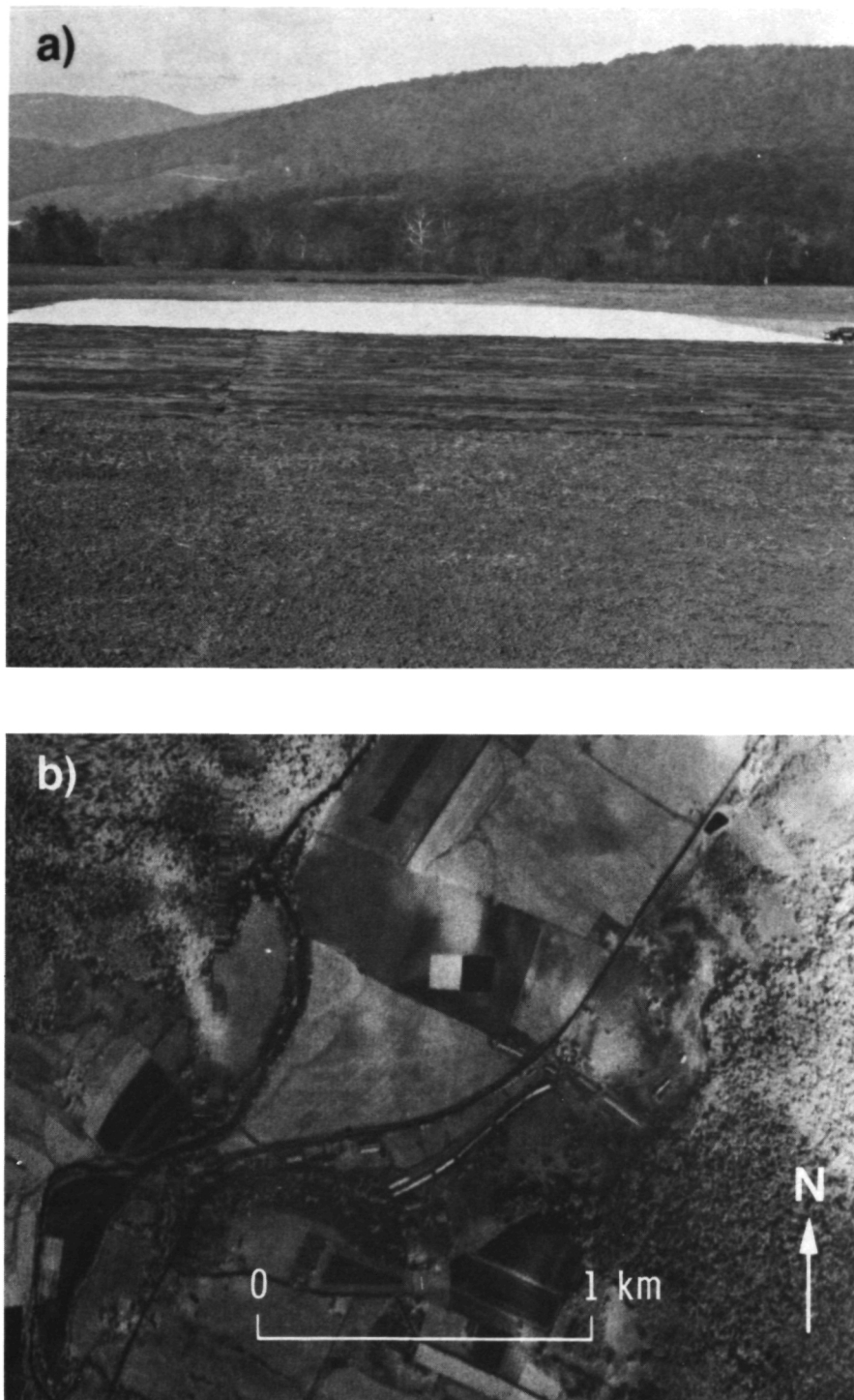


Figure 2. Artificial target deployment at Lost River, West Virginia test site, October 8, 1982: a) ground photograph looking west (note vehicle for scale); b) NS-001 channel 4 (0.76 to 0.90  $\mu\text{m}$ ) image of target. Approximate center of target is longitude  $78^{\circ} 49' 30''$  W, latitude  $38^{\circ} 56' 9''$  N.

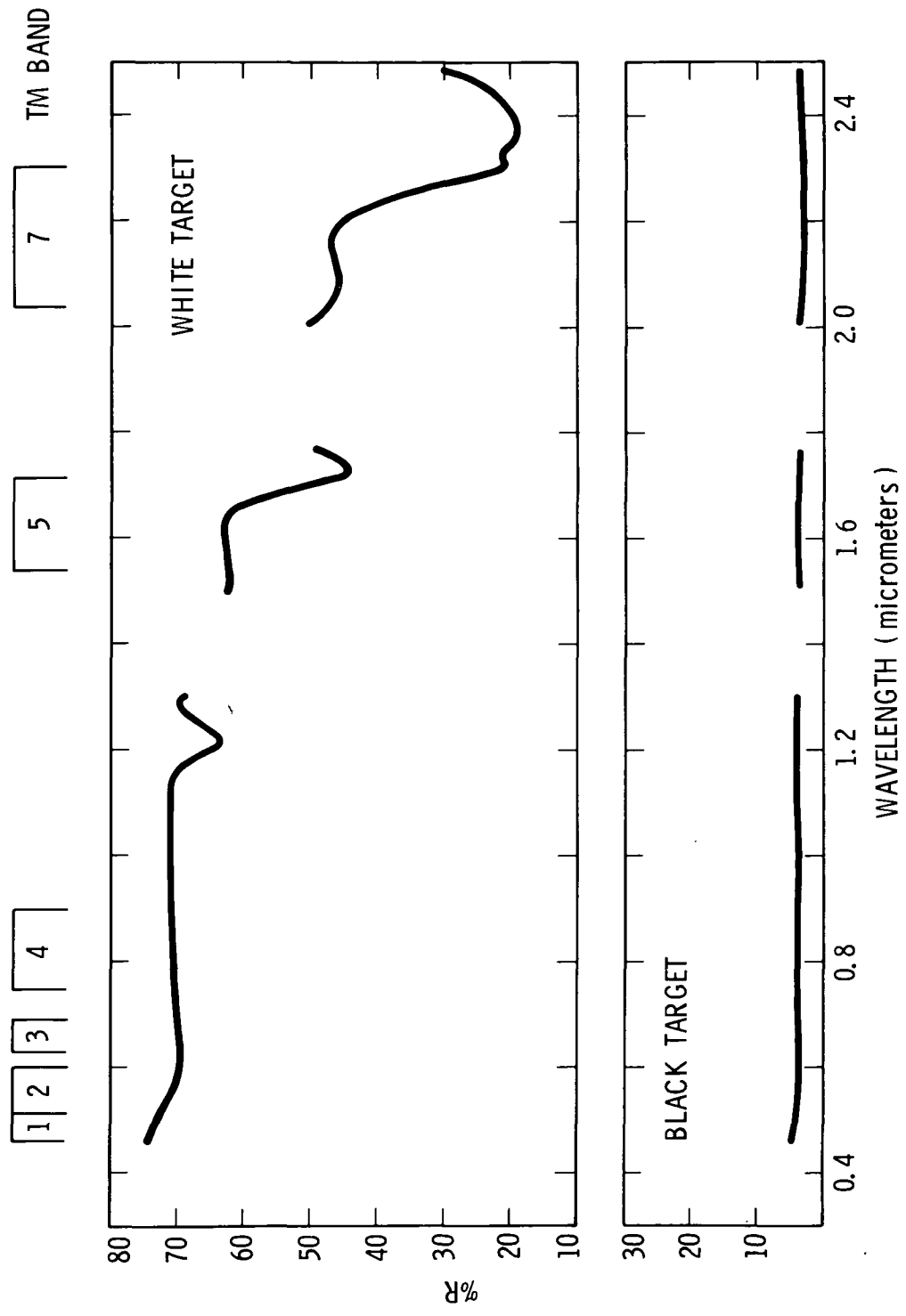


Figure 3. Field spectra of target material obtained with the JPL Portable Field Reflectance Spectrometer (PFRS). Reflectance measurements were also made in the field with the Collins field spectrometer and in the laboratory with the Beckman DK2A and UV5240 spectrophotometers.

Resources allocated for the artificial target experiment were exhausted during the two field deployments. Subsequent calibration studies focused on western test sites where natural ground calibration targets exist. The artificial target experiment demonstrates the feasibility of the method, especially for investigating vegetated sites where typically no appropriate natural calibration targets exist. Target material used in this study is now stored at JPL and is available for use in similar future studies of satellite or aircraft scanner data.

## B) CALIBRATION OF VISIBLE AND NEAR-INFRARED TM DATA

### 1) Background

Satellite radiance data are measures of solar radiation that has been reflected by the Earth's surface and scattered and absorbed by atmospheric gases and aerosols. Of primary interest to geologists are the surface reflectance and the degrading effects on surface reflectance information introduced by atmospheric phenomena. The objectives of this ongoing research are: to provide an empirical relationship between scanner radiance and ground reflectance, allowing interpretation of the satellite data in terms of the surface parameter; to assess the precision with which surface spectral reflectance may be recovered from TM data in the presence of perturbing atmospheric and instrumental factors; and to provide improved theoretical/empirical methods for the correction of atmospheric effects in scanner data. Our approach is field-oriented and utilizes ground observations of surface spectral reflectance with portable spectrometers and radiometers to develop the required empirical relationships.

### 2) Method

Solar radiance incident at the spacecraft has been reflected by the surface and attenuated by the Earth's atmosphere. For a satellite scanner system, operating over locally uniform ground with homogeneous atmosphere above, the upward directed radiance is given by

$$I = I_1 + \frac{R}{1 - R\bar{s}} I_2 \quad (1)$$

where the first term  $I_1$  represents radiation from the atmosphere alone, and the second term signifies radiation that interacts with both the atmosphere and the surface. The uniform Lambertian surface reflectance is  $R$ ,  $\bar{s}$  is a parameter describing the overall probability of backscatter from the atmosphere after reflection by the ground, and  $I_2$  the overall probability of transmission by the atmosphere after reflection by the ground. All quantities in equation (1) are functions of wavelength. The determination of  $R$  from equation (1) requires determination of the functions  $I_1$ ,  $I_2$ , and  $\bar{s}$ . In principle these may be determined by theoretical study of model atmospheres, provided information is available on concentration and distribution of aerosols, as well as the absorbing gas species present. This information is not, however, generally available for the specific times and places of satellite data acquisition.

We provide here an illustration of an alternate method wherein the required parameters of equation (1) are determined empirically using ground-based measurements of spectral reflectance. The image data set used is the TM scene for Wind River Basin, Wyoming (scene ID# 40128-17232, acquired November 1982).

### 3) Results for Surface Spectral Reflectance

Field spectral measurements of surface bidirectional reflectance were made for selected targets throughout the Wind River TM scene using the PFRS (Conel et al., 1985). TM image radiance values, expressed in digital numbers (DN's) were determined for each of the field sites. Scatterplots of image DN versus surface reflectance, averaged over bandpasses of the TM, were prepared (Figure 4). From these it will be recognized that the term  $I_1$  of equation (1) is obtained as the intercept value at  $R = 0$ , and the value of  $I_2$  is obtained from the slope. These plots are found to be linear with correlation coefficients of 0.96 or greater for all channels of the TM.

It is also possible to obtain good fits to the data using parabolic equations. Quasi-parabolic functional behavior would indicate a contribution to the radiance from the multiple reflection factor  $1/(1 - R_s)$  and would provide a means for determining  $s$  directly from the curvature term. Based on careful statistical analysis of possible fits to the data, the presence of nonlinear terms in equation (1) cannot be established. For the atmospheric conditions prevailing during the time of the satellite data acquisition we conclude that the appropriate form of equation (1) is the linearized version

$$I \approx I_1 + I_2 R \quad (2)$$

An approximate determination of  $s$  is still possible for the specific model of an isotropically scattering, homogeneous atmosphere. This requires interpretation of the functions  $I_1$  and  $I_2$  in terms of an optical depth and a single scattering albedo. These determinations will be discussed further below.

For determination of surface (bi-directional) reflectance from the TM image DN data, all that is now required are the graphical forms in Figure 4 or equivalent analytical expressions given by equation (1) interpreted in terms of the DN.

To illustrate the application of this method to determination of ground reflectance, we present a comparison between image-derived spectra and measured field reflectance spectra for five areas throughout the Wind River TM scene. None of the areas were used in production of the calibration curves (Figure 4). Figure 5 gives the spectral distribution of raw DN values and Figure 6 the image and field spectra for selected test areas. The chronology of events was as follows: (1) the original TM scene was obtained in November 1982; (2) field measurements were obtained in November 1983 and were used to construct the calibration lines of Figure 4; and (3) field measurements of the additional "unknown" areas were obtained in July 1984. Thus, the comparisons (unavoidably) involve measurements spanning a period of approximately two years.

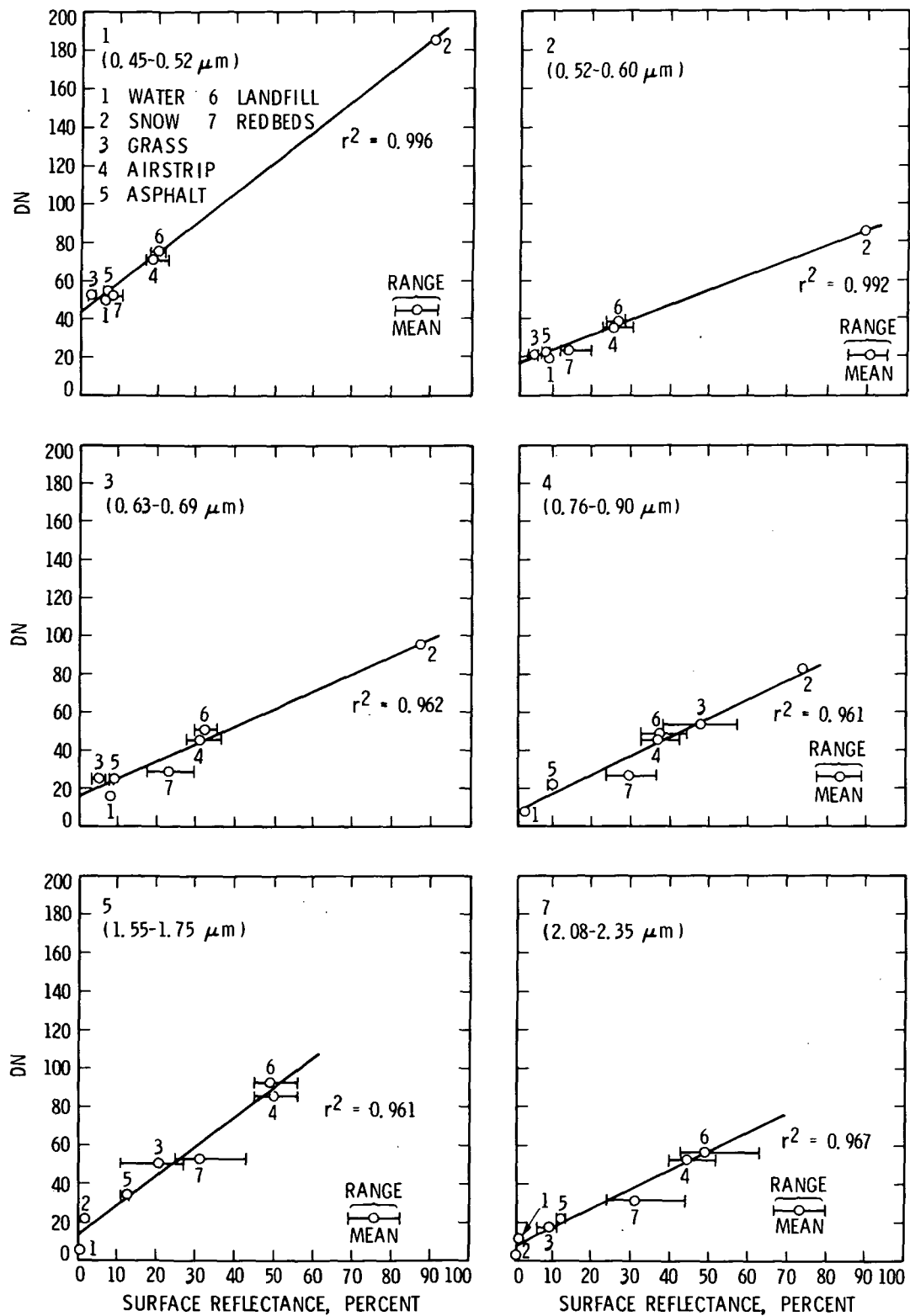
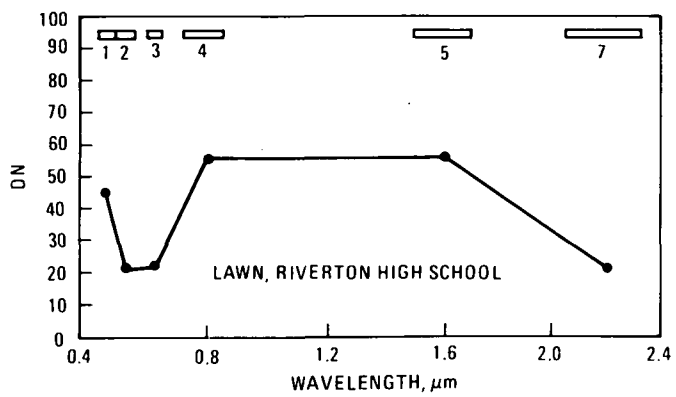
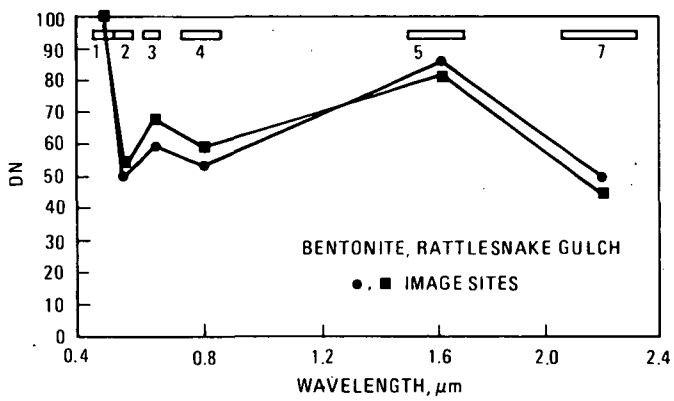
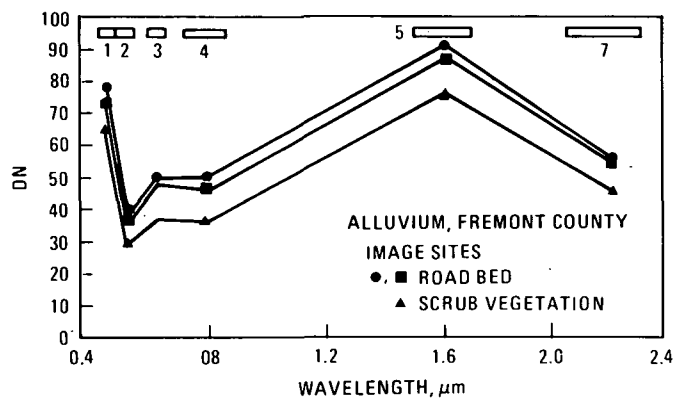
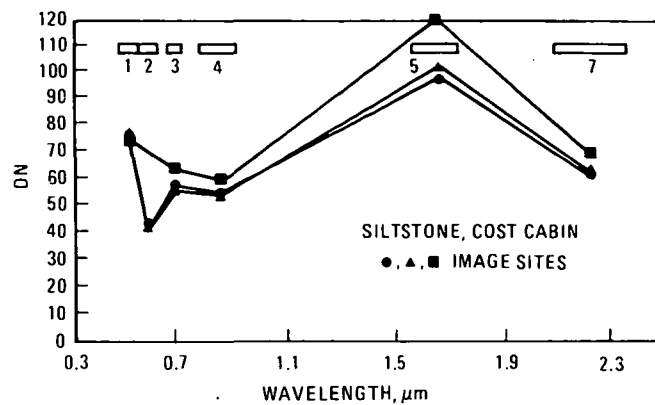
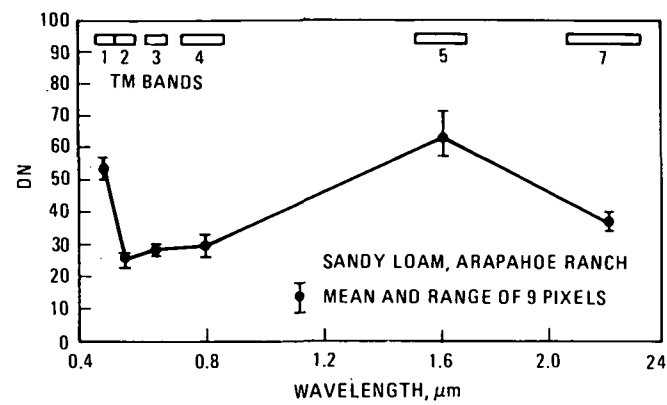
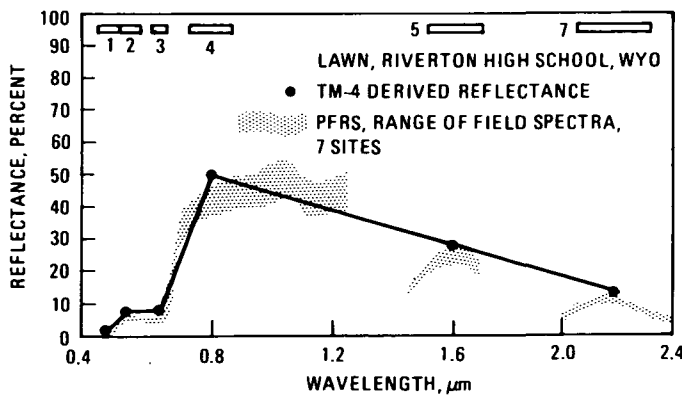
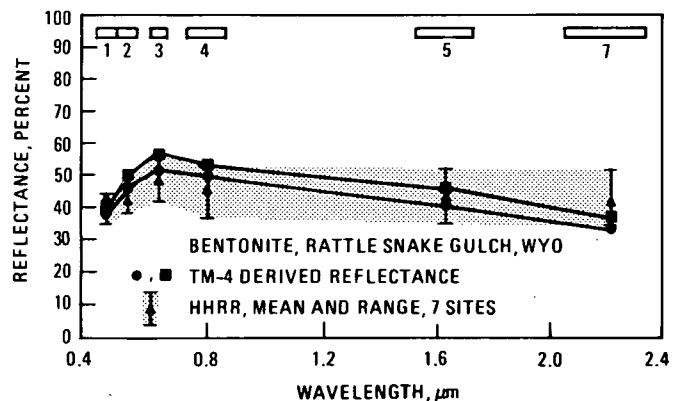
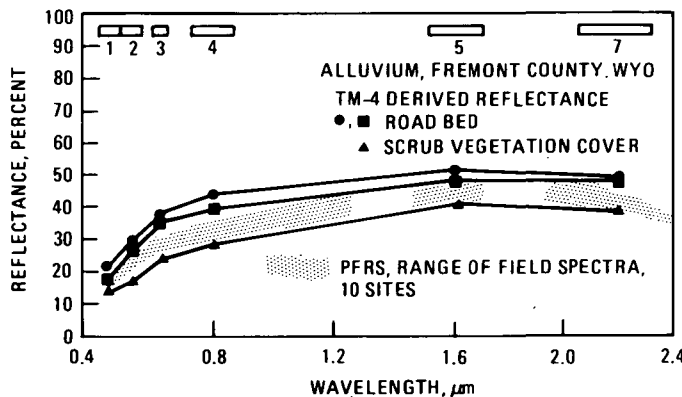
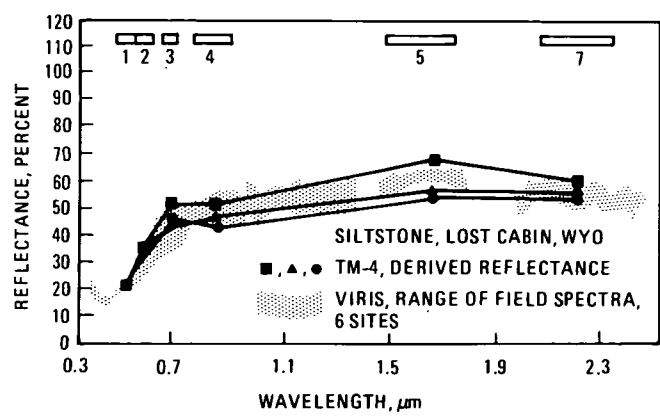
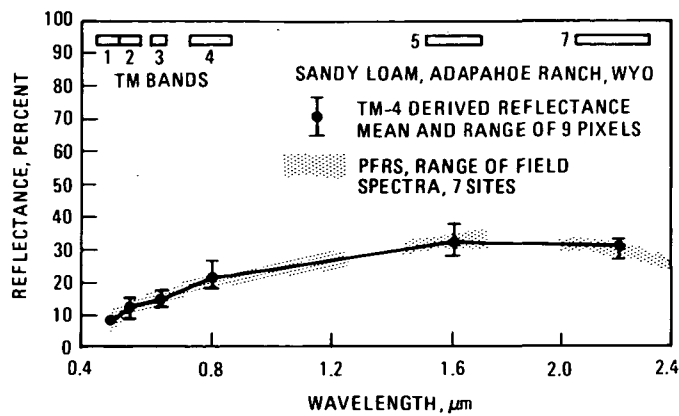


**Figure 4.** Distribution of image DN vs. surface reflectance for bands 1, 2, 3, 4, 5, and 7. Data was obtained from the Landsat-4 TM scene of Wind River Basin, Wyoming, November 21, 1982.



TM-4 DATA ACQUIRED, NOV., 1982

Figure 5. Raw DN values of Landsat-4 TM data, Wind River Basin, Wyoming, for selected ground targets.



TM-4 IMAGE CALIBRATION, NOV., 1983  
FIELD SPECTRAL DATA REQUIRED JULY, 1984

Figure 6. Calibrated Landsat-4 TM image reflectance spectra for selected sites in the Wind River Basin, Wyoming. Equivalent field reflectance spectra are also shown for comparison.

In general terms, agreement between the two sets of observations is excellent to good, and there is every reason to expect that the comparisons could be improved if the time interval between satellite and field measurements could be shortened. In addition to this logistical difficulty, two additional problems must be routinely addressed. First, the field sites were chosen because they were homogeneous and (except for Riverton High School lawn) unvegetated. Despite careful selection, the targets are not completely homogeneous, and we must rely upon a limited sampling to provide representative reflectance data. Second, the targets are often only a few pixels in size and it is often difficult to locate them with complete accuracy in the images.

Problems that are likely to contribute second order effects include those of so-called adjacency effects, the surface phase function, and the comparison of bi-directional versus Lambertian surface reflectance functions. Adjacency effects, introduced by the atmosphere in spectral regions where scattering is important, act to reduce contrasts in image data between adjacent areas of differing surface reflectance. Kaufman and Joseph (1982) have provided some numerical examples. These problems can be minimized by working far from the boundaries of large areas of differing albedo, but this is not usually possible in practice. For optically thin conditions, with optical depth on the order of 0.1 or less, the effects may amount to a relative change in brightness of less than a percent (Kaufman and Joseph, 1982, Figure 3). Relative effects of this magnitude will be difficult to detect, let alone correct for in the image data. The adjacency effect in the image data acts so that bright areas will decrease in brightness relative to surrounding darker areas, and the brightness of darker terrain will be increased. These effects will influence both the calibration relationships as well as the determined brightness values for isolated pixels in the scene. The second problem can be minimized by taking field measurements at the same phase angle and solar elevation as the satellite observations. The third problem is not considered to be a serious difficulty for the present observations since the atmosphere, especially at longer wavelengths, was optically thin.

Considering all these complications, the agreement between measured and satellite-determined reflectance properties is remarkably good. This lends support to the assumption, implicit in equation (1), of essentially image-wide atmospheric homogeneity during satellite data acquisition.

#### 4) Determination of Atmospheric Parameters

The actual scattering properties of the atmosphere together with optical depth may be determined from the functional relationships  $I_1$  and  $I_2$ . For the homogeneous atmospheric model given by Chandrasekhar (1960)

$$I_1 = \frac{F}{4\mu} S(\mu, \phi; \mu_o, \phi_o) \quad (3)$$

and

$$I_2 = F\mu_o \gamma_1(\mu) \gamma_1(\mu_o) \quad (4)$$

where the functions  $S(\mu, \phi; \mu_o, \phi_o)$  and  $\gamma(\mu)$  are defined in the reference cited. In equations (3) and (4),  $F$  is the incident solar irradiance and  $\mu$ ,  $\phi$ ,  $\mu_o$ , and  $\phi_o$  represent incidence and viewing directions respectively. For an optically thin atmosphere the expressions for  $S(\mu, \phi; \mu_o, \phi_o)$  and  $\gamma(\mu)$  simplify greatly. In particular, the expressions for  $I_1$  and  $I_2$  reduce to

$$I_1 = \frac{F}{4\pi\mu} \left( \frac{1}{\mu} + \frac{1}{\mu_o} \right)^{-1} p(\mu, \mu_o) \left\{ 1 - e^{-\tau} \left( \frac{1}{\mu} + \frac{1}{\mu_o} \right) \right\} \quad (5)$$

and

$$I_2 = \frac{F}{\pi} \mu_o e^{-\tau} \left( \frac{1}{\mu} + \frac{1}{\mu_o} \right) \quad (6)$$

where  $p(\mu, \mu_o)$  is the scattering phase function between the directions of incidence and observation and  $\tau$  is the optical depth. Thus, equation (6) may be solved for  $\tau$  and used in equation (5) to obtain  $p(\mu, \mu_o)$ . The results of such calculations for the values of  $I_1$  and  $I_2$  obtained from Figure 4 are given in Figures 7 and 8. Here the error bars are determined by the standard least square errors of the intercept and slope values in Figure 4 for the functional forms of equations (5) and (6), specifically

$$\sigma_\tau = \left( \frac{\partial \tau}{\partial I_2} \right) \sigma_{I_2} \quad (7)$$

and

$$\sigma_p^2 = \left( \frac{\partial p}{\partial I_1} \right)^2 \sigma_{I_1}^2 + \left( \frac{\partial p}{\partial \tau} \right)^2 \left( \frac{\partial \tau}{\partial I_2} \right)^2 \sigma_{I_2}^2 \quad (8)$$

The error in determination of optical depth is smaller than that of the phase function. This derives ultimately from the fact that the standard error in the least square determination in slope of the calibration lines is less than the standard error of determining the intercept value.

### 5) Estimate of the Parameter $\bar{s}$

The parameter  $\bar{s}$  describes the backscatter of atmospheric radiation reflected from the surface. It is expected to have a wavelength dependence similar to  $S(\mu, \phi; \mu_o, \phi_o)$ , since this latter function describes the reflection of light from the atmosphere alone (i.e.,  $R = 0$ ). Analyses of the data in Figure 4 suggest the nonlinear terms represented by the factor  $1/(1 - R\bar{s})$  are small, but the presence or absence of curvature, especially in bands 1, 2, 3, and 4, is completely determined by the plotted reflectance and DN values for snow. We were not able to obtain in situ snow measurements during TM data acquisition in November, 1982 and instead used representative snow values from an extensive library of PFRS reflectance spectra at JPL. Likewise, we choose a representative snow radiance measurement from the Wind River TM scene. Thus, the snow points in Figure 4 are the least well constrained of any contained in those graphs.

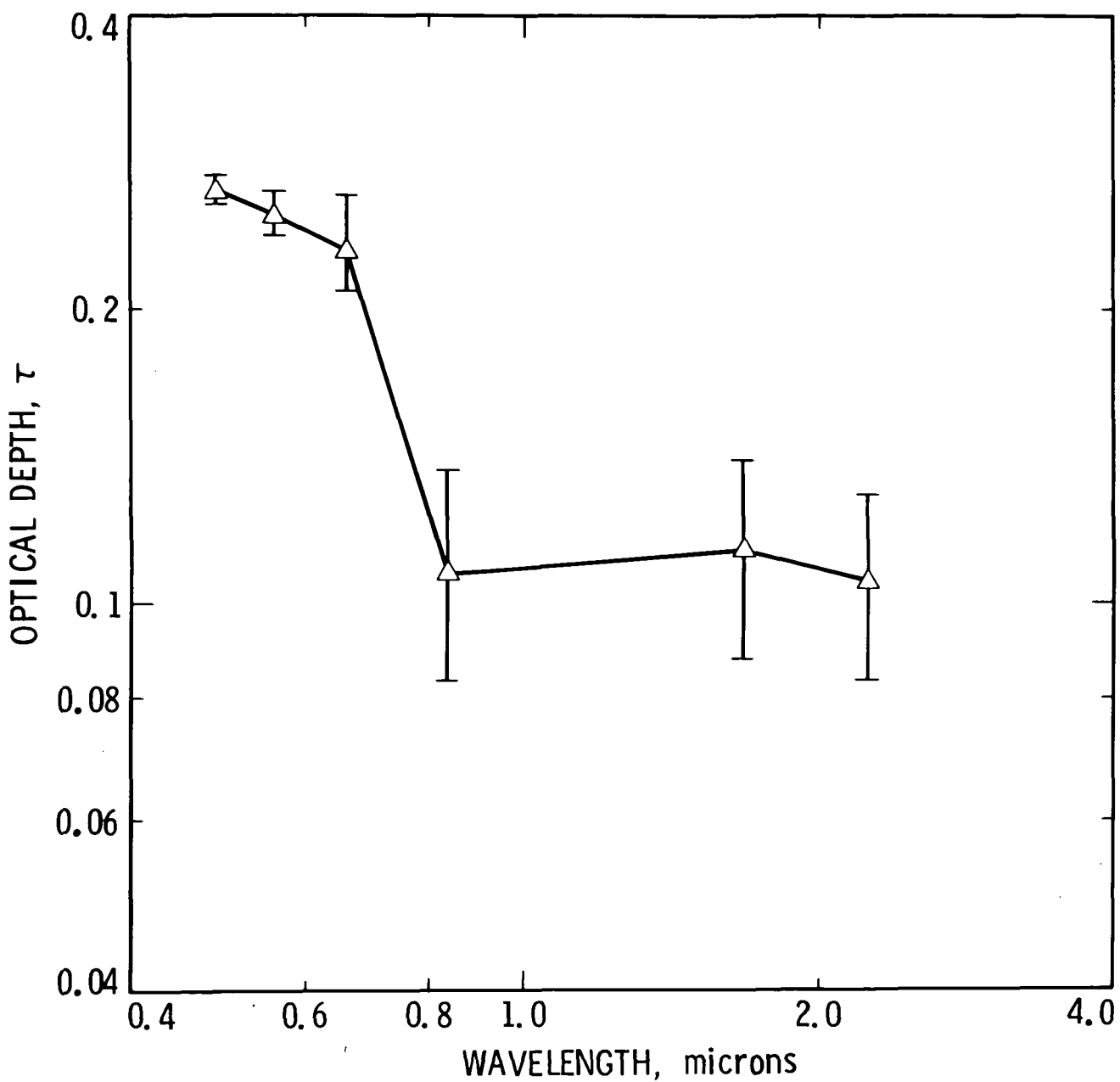


Figure 7. Optical depth as derived from the function  $I_2$ .

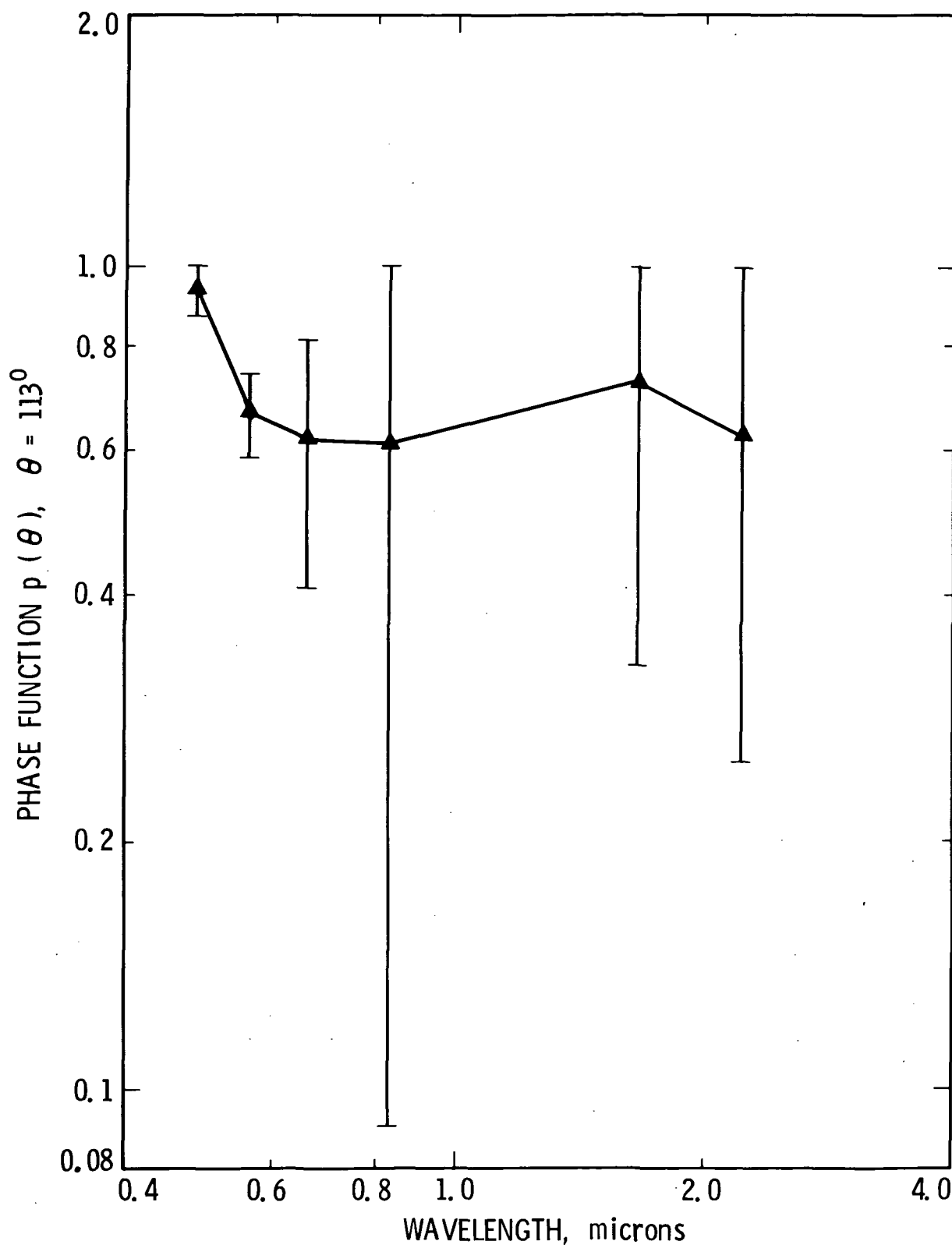


Figure 8. The phase function  $p(\theta)$  determined for the phase angle  $\theta = 113^\circ$  and the functions  $I_1$  and  $I_2$ .

It is still possible to obtain an estimate of  $\bar{s}$  by assuming the atmosphere to be homogeneous and isotropically scattering and using theoretical calculations of Chandrasekhar and Elbert (1952), together with our previous estimates of the single-scattering phase function and the optical depth. In this instance it is required to interpret the phase function as the single-scattering albedo. Real atmospheric aerosols do not scatter isotropically, but the simple isotropic approximation is useful to illustrate the nature of the effects introduced.

The wavelength dependence of  $\bar{s}$  determined from tables in Chandrasekhar and Elbert (1952) for our values of  $p$  and  $\tau$  is shown in Figure 9. This function is closely correlated with  $S(\mu, \phi; \mu_0, \phi_0)$  as may be seen in Figure 10.

The magnitude of the effect to be expected from the factor  $1/(1 - R_s)$  on calibration equation (2) may be seen by replottedting the equation using this factor. These two forms are compared in Figure 11. The largest differences between the linear and nonlinear equations occur at higher surface reflectance, especially in bands 1, 2, 3, and 5. Thus, curvature is most easily established by securing reflectance determinations within a range of reflectance values, intermediate to low and high values (for example in band 1, 20 to 90%). Apart from snow and artificial targets, however, surfaces with these reflectance values are rare on the earth's surface.

#### 6) Application to the Determination of the Atmospheric Modulation Transfer Function (MTF)

The atmospheric MTF describes attenuation of light reflected by the surface and directly transmitted by the atmosphere as well as the effect of light reflected from the surface and diffusely transmitted by the atmosphere. The diffuse component tends to decrease the radiance above bright targets and to increase the radiance above dark targets. A discussion of these problems is presented by Kaufman (1984). Correcting for these effects improves contrasts between areas of differing albedo in the image data. The present discussion illustrates how data derived from our field measurements may be used to construct MTF's for the image independently of any theoretical calculation of radiances or other parameters.

The atmospheric MTF is defined by the ratio (Kaufman, 1984)

$$M(k_x, k_y) = F(I(x, y) - I_0)/F(A(x, y)) \quad (9)$$

where  $F$  represents the Fourier transform,  $A(x, y)$  is the surface reflectance at position  $(x, y)$ ,  $I(x, y)$  is the upward-directed radiance outside the Earth's atmosphere, and  $I_0$  is the radiance from the atmosphere alone. All quantities are normalized to reflectance units. The numbers  $k_x$  and  $k_y$  represent spatial frequencies. In terms of upward radiance at the surface without the atmosphere present,  $I_e$ , the radiance outside the atmosphere is

$$I(x) = F^{-1}(F(I_e(x))M(k)) + I_B + I_0 \quad (10)$$

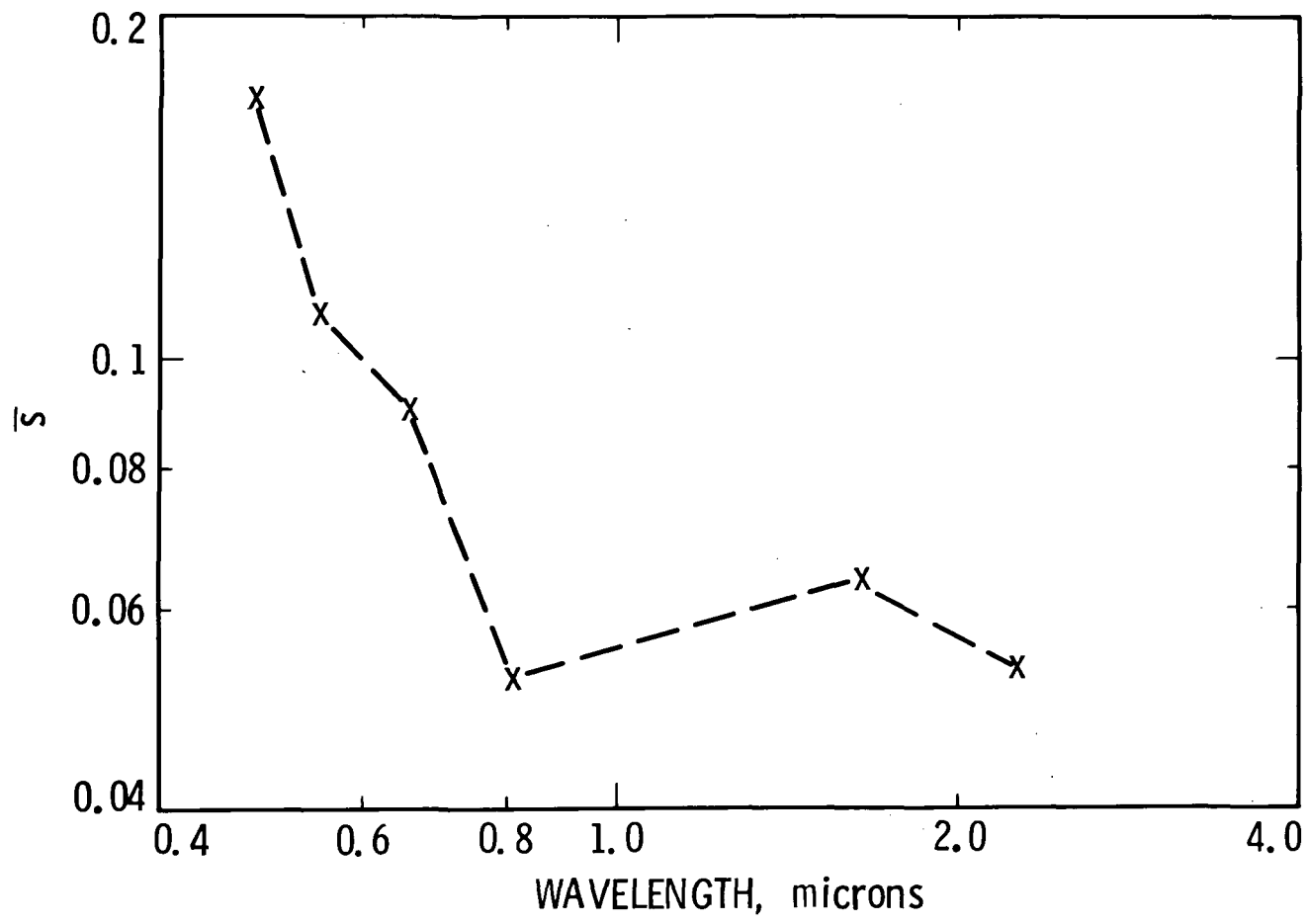


Figure 9. The backscatter function  $\bar{s}$ , determined under assumption of isotropic scattering for the optical depth and single-scattering albedo derived previously.

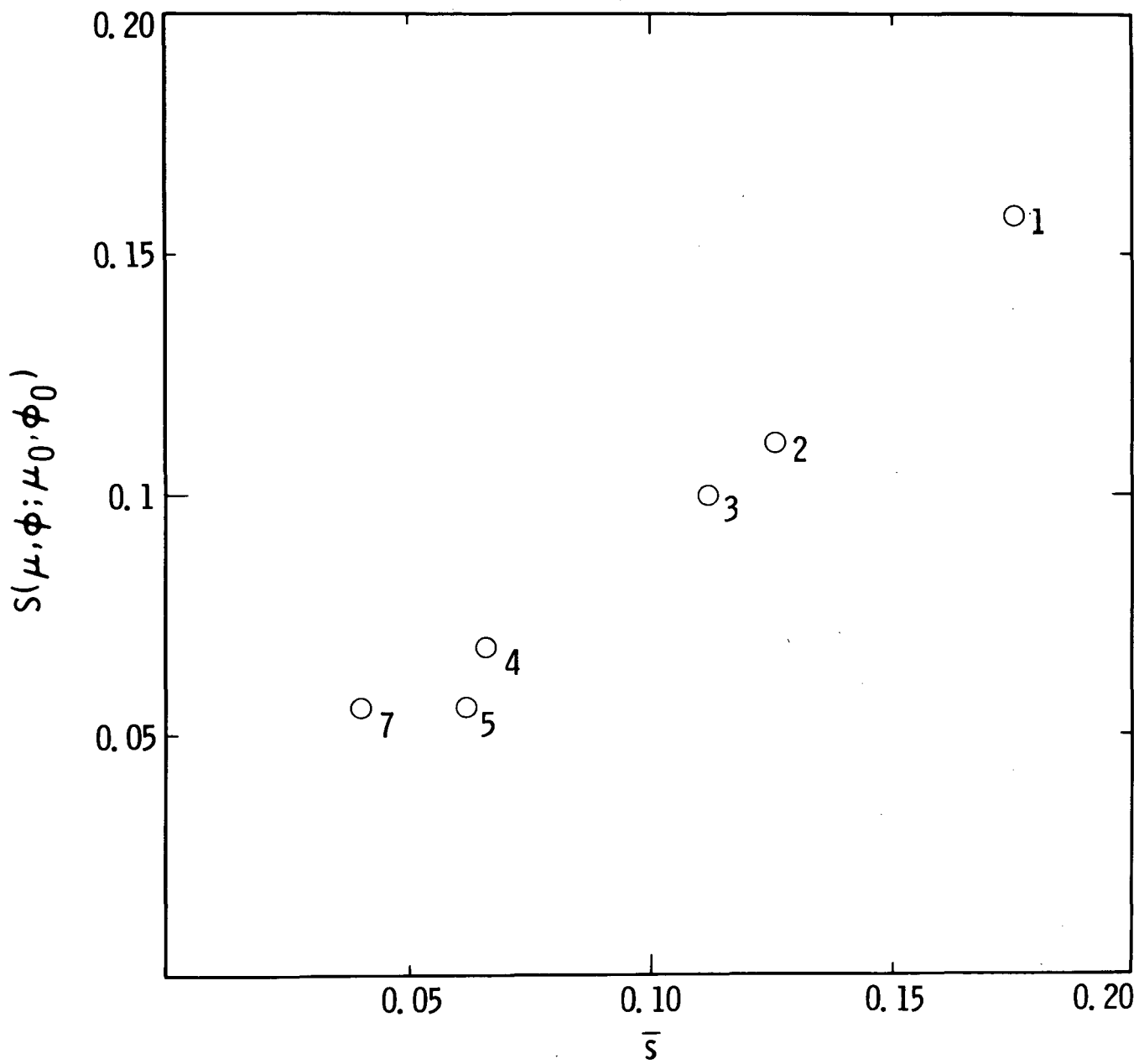


Figure 10. Correlation of the functions  $S(\mu, \phi; \mu_0, \phi_0)$  and  $\bar{s}$ .  
Numbers refer to TM bands.

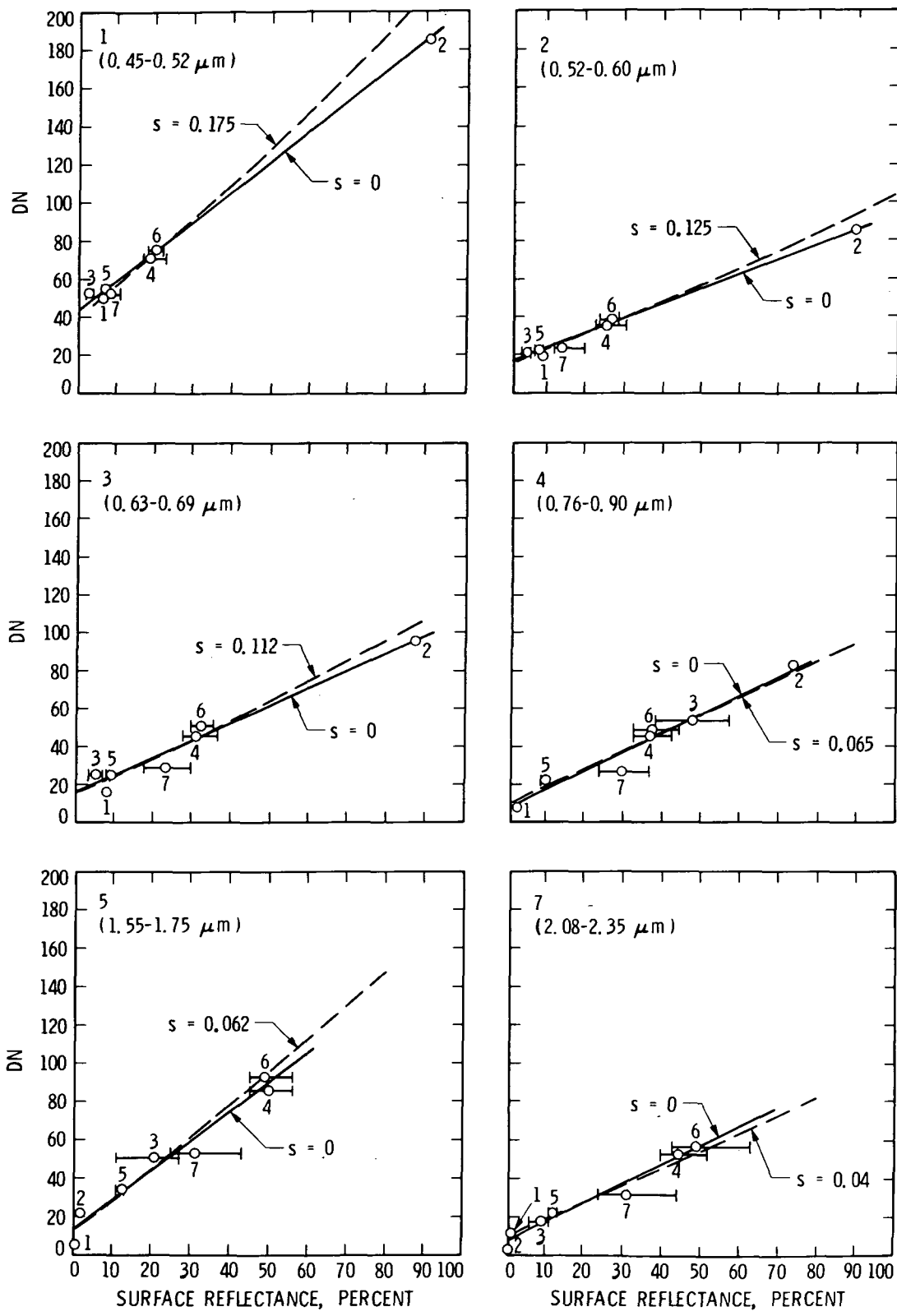


Figure 11. Calibration runs obtained by inclusion of the multiple scattering term  $1/(1-R s)$  in the relationship between scanner radiance (DN) and surface reflectance (R). Values of  $s$  used are given in Figure 10.

The term  $I_\beta$  represents radiance from the downward-directed backward scattering from the atmosphere, resulting from large-scale horizontal interactions. Model calculations of the magnitude of  $I_\beta$  show its effect on the MTF to be negligible (Kaufman 1982, Table 4). Inverting the above equation for  $I_e$

$$I_e(x) = F^{-1} (F(I(x) - I_\beta - I_0)/M(k)) \quad (11)$$

where  $x$  represents a two-dimensional coordinate. It may now be realized that all quantities required to secure the image MTF, local or otherwise, are obtainable from our previous calibration procedure and atmospheric analysis. In particular, the quantity  $I_0$  is equivalent to our  $I_1$  (equation 1); the albedo  $A(x,y)$  is obtained by application of the calibration equations with their empirically derived constants. Thus, the MTF may be calculated from equation (9) and used together with the observed radiances  $I(x)$  to compute  $I_e$  from equation (11).

## 7) Discussion

An approximate analysis of the atmospheric attenuation problem has been employed to demonstrate the utility of empirical/theoretical procedures for obtaining surface reflectance data, estimating atmospheric parameters, and constructing atmospheric MTF's. These will be useful for correction of image data for the blurring effects introduced by diffuse scattering and attenuation. All of the applications described have been derived from analysis of the Wind River TM scene. The characteristic of this scene is optically thin atmospheric conditions and apparent horizontal uniformity of the atmosphere. We have utilized a scene-wide set of surface observations to characterize the entire image and, hence, have not been able to address the question of possible lateral variations in atmospheric attenuation directly.

It is still possible, however, to use the method described here to address this problem. The requirement is to find local targets and prepare local calibration curves for a number of sites throughout the scene. The resulting set of observations, each for a specific surface-viewing direction, can then be used to determine variations from place to place in the actual atmospheric radiance and attenuation. This method, while field-labor intensive, is direct, in the sense that the surface albedo variation is eliminated as an unknown in the analysis. The method is not limited to thin atmospheres for its application, but can be applied wherever suitable calibration targets can be found. Calculation of actual atmospheric parameters is, of course, another matter. While we have not discussed the problem of multiple scattering and its effect on the calculated values of phase function and optical depth, the inclusion of such effects, at least to consideration of two or perhaps three scattering events, is relatively straightforward in principle. The approach is to include higher order "correction" terms in the analytic approximations to the X- and Y-functions that are combined to form the functions  $S(\mu, \phi; \mu_o, \phi_o)$  and  $Y(\mu)$ . The resulting equations are polynomials in the single-scattering albedo and optical depth, the roots of which must be sorted out to obtain the appropriate corrected values of the parameters sought.

### C) DYNAMIC RANGE OF THE TM SYSTEM

Histograms showing DN distributions for each band of the Wind River Basin TM scene were constructed from SCRUNGE-processed, P-tape image data acquired November 21, 1982 (path 36, row 30, ID # 40128-17232). Inspection of the histograms (Figure 12) provides insight on the radiometric characteristics of these Landsat-4 TM data. DN's for bands 1, 3, 4, and 5 range from 0 to 255; the maximum in bands 2 and 7 is less than 255 DN. Ninety-eight percent of the data fall within the range from 4 DN (band 7) to 234 DN (band 1). Mean values range from 29 DN (band 7) to 75 DN (band 1); standard deviations range from 16 DN (band 7) to 49 DN (band 1).

The most apparent feature of these histograms is the narrow DN distribution recorded for superficial materials of interest to earth science. Except for band 1, the range of DN's recorded for (diffuse-reflecting) water, vegetation, soils and rock, and snow utilize less than one half of the 256 DN's available. A substantial portion of the DN range in all bands, except band 1, is occupied by clouds. Specularly reflecting snow occupies most of the upper DN range in bands 2, 3, and 4.

Examination of histograms for six other Landsat-4 TM scenes revealed similar narrow DN ranges (Figure 13). Townshend et al. (1983, p. 818) noted narrow DN distributions in an August Landsat-4 TM scene covering Arkansas-Missouri: "For example for band 2, over 95 per cent [sic] of the pixels are found within 25 out of the 256 available digital counts." "Average" histograms provided by a GSFC-EROS Data Center evaluation of 60 Landsat-4 TM scenes "selected to include variations in season, content (land, water, urban, agriculture, etc.), and geographical location" (NOAA, 1983) display similar narrow ranges. These observations lead to the conclusion that histograms for the Wind River scene are typical of Landsat-4 TM data. Such narrow DN distributions imply that the Landsat-4 TM system is not properly configured to fully utilize the 256-DN range available for earth science applications.

Poor utilization of the dynamic range results in degraded resolution of reflectances and low-contrast among natural ground targets. The just-resolvable reflectance difference  $\Delta\rho_i$  obtainable, determined by the quantization of the scanner radiance measured in the DN interval  $\Delta(DN_i)$ , is given by

$$\Delta\rho_i = \frac{d\rho_i}{dDN_i} \Delta(DN_i) \quad (12)$$

where the derivative is the slope of the calibration curve for the  $i^{\text{th}}$  TM channel. Improved resolution is clearly obtained by increasing the DN range, or by decreasing  $d\rho_i/dDN_i$

The resolvable spectral reflectance differences clearly affect the quality of the acquired images, as well as images based on transformations of the data. For example, the just-resolvable differences in principal components ( $\Delta PC_i$ ) are obtained from  $\Delta PC_i = \sum_j \lambda_{ij} \Delta(DN_j)$ , where the  $\lambda_{ij}$  are components of the eigenvectors.  $j$

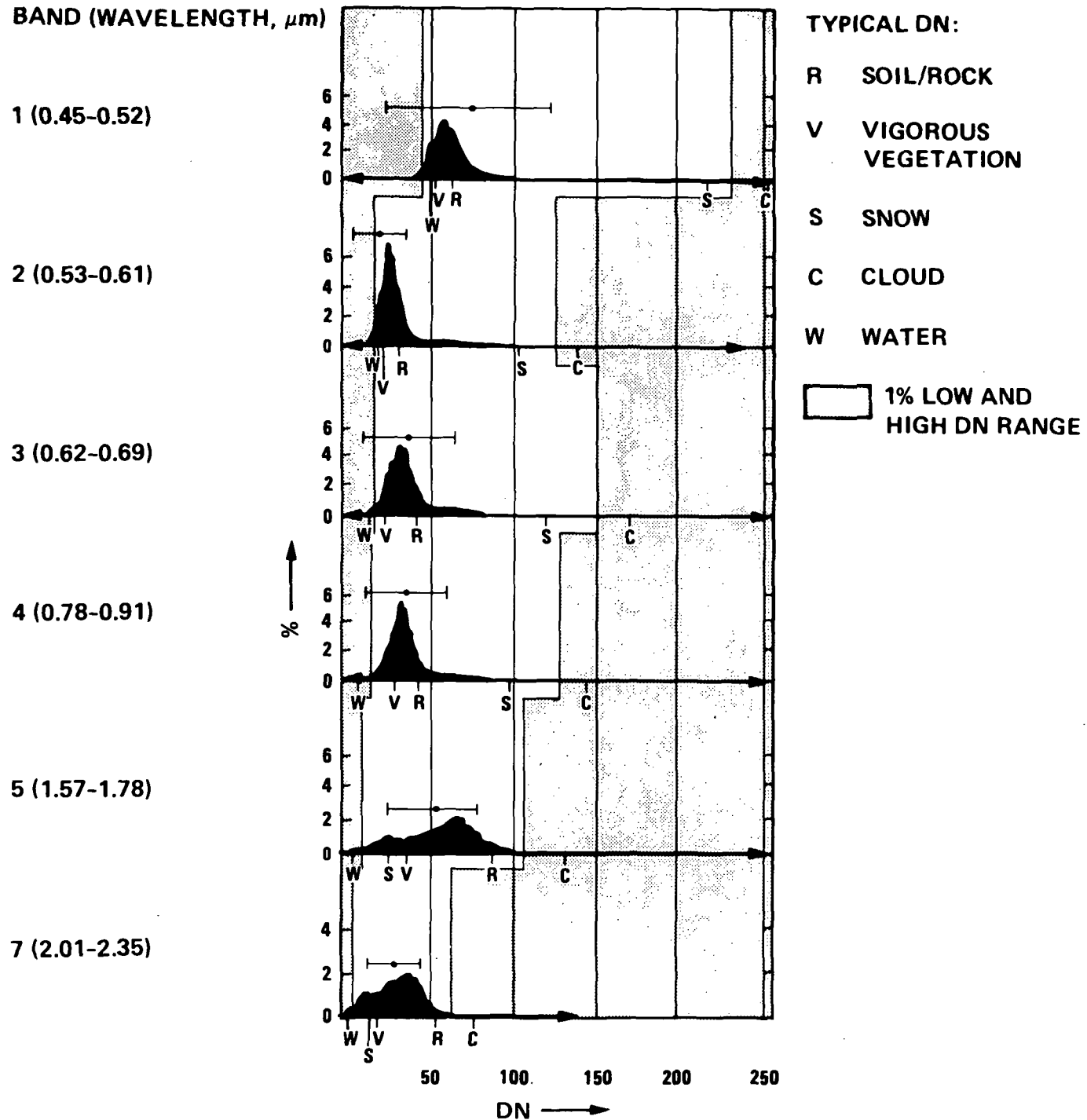


Figure 12. Histograms for the Landsat-4 TM image covering the Wind River Basin area, Wyoming. Mean values are indicated by a dot on standard deviation error bars. Arrows indicate maximum and minimum DN. Position of the 1% cutoff, relative to the 1 sigma value, reflect the highly skewed, non-gaussian distribution of DN values for this scene.

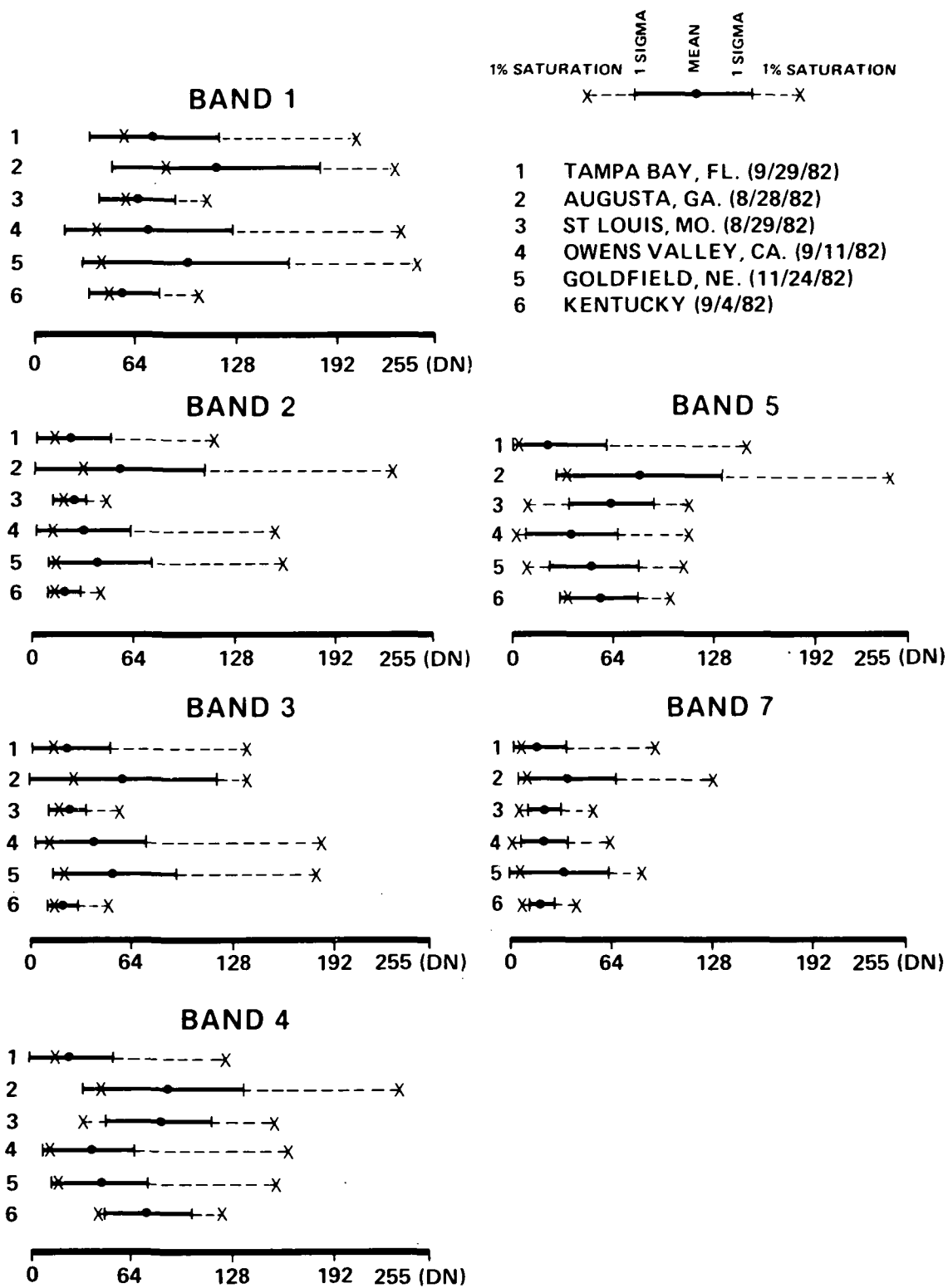


Figure 13. DN distributions for six Landsat-4 TM scenes. Note narrow DN distributions similar to those of Figure 12. The higher DN ranges of some (for example Augusta, GA) is attributed to clouds in the scene.

## 1) Radiometric Comparison of A-, B-, and P-Format TM Data

A-, B-, and P-format data of the Wind River Basin, Wyoming TM scene were compared for radiometric differences. B-format data are essentially raw, with no corrections applied either geometrically or radiometrically: the data are dominated by interdetector response differences and a 16-line, 45 to 50 pixel offset associated with forward and reverse scans of the TM. A-format data are corrected radiometrically to remove interdetector differences, but are geometrically the same as B-format data. P-format data are corrected both radiometrically and geometrically. DN frequency distributions (histograms) of each band reveal that B-format data yield histograms with the most structure or frequency-variability. The structure appears as a high-frequency (wavelength of 4 to 8 DN's) cycling, with an amplitude of approximately 30 to 40 percent of the total DN distribution at that interval. The origin of these variations is most likely differences in the response of the detectors in the arrays. A-format data (radiometrically corrected) exhibit less histogram structure; band means and standard deviations are higher by 1 DN than those of the B-format data. P-format data have the "smoothest" histograms, and the means and standard deviations in each band are generally 2 DN's lower than those of the A-format data. Based on these minor differences in frequency distribution, no significant radiometric degradation occurs during correction from raw data to radiometrically and geometrically corrected data.

Atmospheric calibration of A- and B-format data offers an additional means of comparison to P-format data. The calibration procedure for these data is identical to that discussed earlier for P-format data. Identification of calibration targets is more difficult due to the 16-line, 45 to 50 pixel offset associated with forward and reverse scans by the TM sensor. In spite of this problem, only one (grass) of the seven targets used in calibrating P-format data could not be identified. Regression parameters derived from six-point fits of these A- and B-format data are summarized in Table I, along with P-format, 7-point fit parameters. The similarity in A-, B-, and P-format regression parameters further supports the conclusion that no significant radiometric changes occur in the TM data as a result of radiometric and geometric corrections by SCRUNGE processing.

## 2) Landsat-4 TM Gains and Offsets: Sensitivity Analysis of TM Radiometry Based Upon Wind River Data

The calibration data summarized in Figure 4 and Table I suggest specific increases in gains and offsets to optimize the data for earth science applications. For example, in Landsat-4 TM band 2, ground targets having zero reflectance are recorded at 16 DN; targets having 100 percent reflectance are recorded at 93 DN. Only 77 DN's (about 6 bits) are actually utilized for recording diffuse reflecting ground targets in the Wind River TM scene. The remaining 179 DN's of the 8-bit data record specular reflectance from snow, diffuse reflectance from snow and clouds, and possibly noise (Figure 12). Clearly, the present gain and offset settings of the Landsat-4 TM sensor underfill the 8-bit record.

Table I. Comparison of A-, B-, and P-format calibration parameters of TM data in the Wind River Basin, Wyoming.

Format	Band	Gain	Offset	R-Squared
B	1	1.50	42.29	0.999
	2	0.71	14.13	0.992
	3	0.93	12.87	0.996
	4	0.92	7.81	0.963
	5	1.42	13.48	0.953
	7	0.96	6.19	0.960
A	1	1.52	41.46	0.999
	2	0.73	14.65	0.991
	3	0.94	16.63	0.967
	4	0.95	7.23	0.957
	5	1.49	13.39	0.958
	7	0.99	6.05	0.963
P	1	1.55	43.15	0.996
	2	0.77	15.83	0.991
	3	0.92	15.38	0.961
	4	0.99	7.15	0.960
	5	1.53	13.15	0.961
	7	0.99	7.57	0.966

If the gain and offset were increased so that a ground target of zero diffuse reflectance were recorded as 0 DN, and a target with 100 percent diffuse reflectance were recorded as 255 DN, the possible range of diffuse ground reflectances would occupy 256 gray levels. Using this criterion and calibration data summarized in Figure 4 and Table I, optimal gain and offset increases for the 6 Visible and Near Infrared (VNIR) bands of the TM sensor were calculated (Figure 14). The suggested offset increases range from 6 DN's (band 4) to 44 DN's (band 1); gain increases range from 1.63 (band 1) to 3.29 (band 2).

The specific increases suggested will significantly improve the useable dynamic range for study of water, vegetation, soil, rock, and cultural features under similar illumination conditions. Utility of the data for study of diffuse-reflecting snow and ice would be reduced, primarily in bands 1, 2, 3, and 4, at low latitudes in summer months.

### 3) Sensitivity of TM Radiometry Based Upon Preflight Laboratory Calibration Data

The qualitative results described above argue that the Landsat-4 TM system does not deliver 8-bit ground reflectance data for the kinds of targets of interest to geologists or under the illumination conditions of the Wind River scene. The following quantitative analysis of the TM system based upon preflight laboratory calibration data also validates these results.

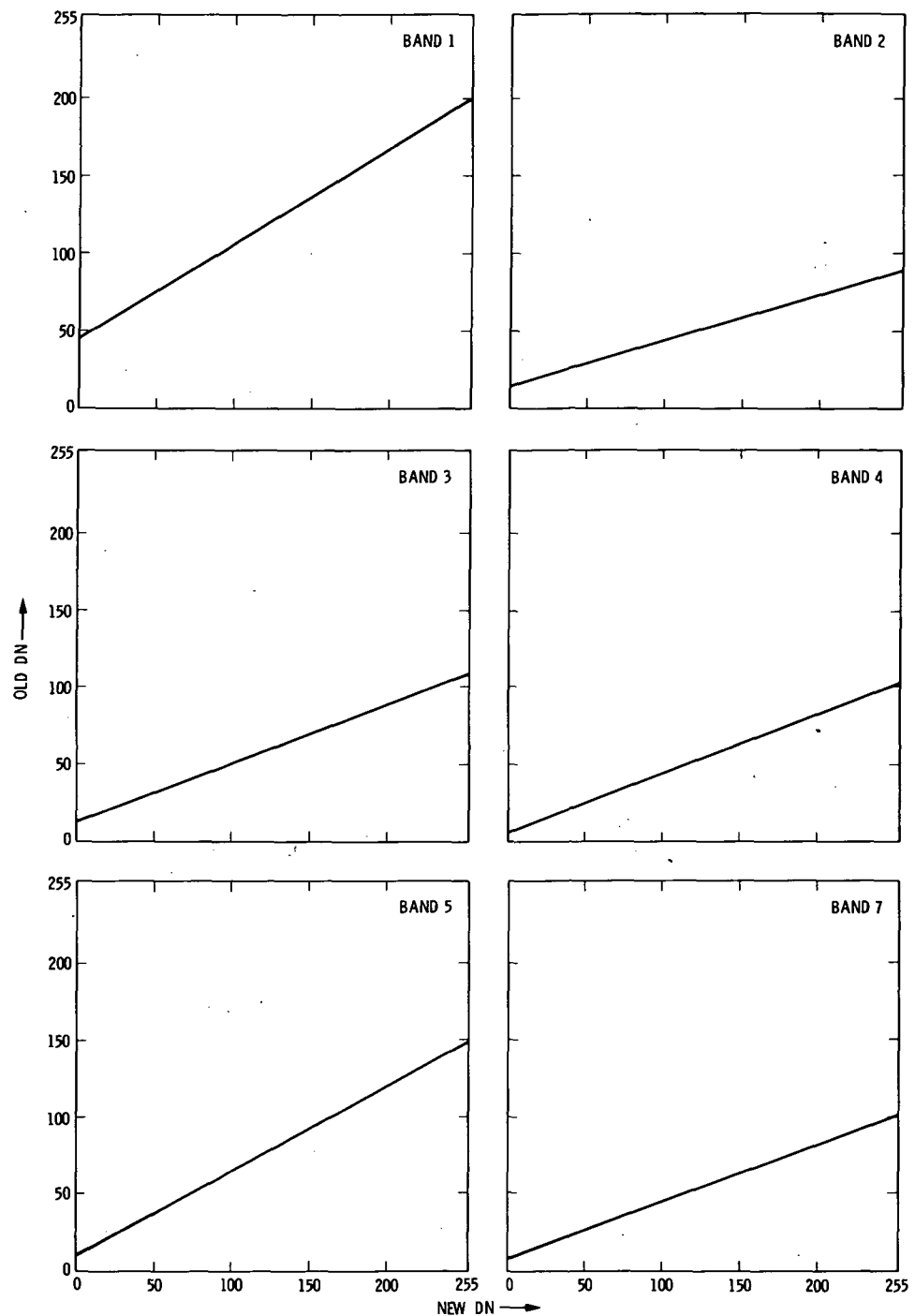
Equation (1) is the basis for determining what differences in spectral reflectance  $\Delta R$  may be obtained from TM scanner data, including effects of both the atmosphere and the precision of scanner radiance measurements  $\Delta I$ . In particular,

$$\Delta I = I_2 \Delta R / (1 - \bar{R}_s)^2 \quad (13)$$

Accurate measurement of  $I_2$  is thus required together with a knowledge of  $\bar{s}$ . From equation (13) the largest uncertainty in  $R$  for a given value of  $\Delta I$  occurs at the largest values of the reflectance. The TM system signal-to-noise ratio (i.e.,  $I/\Delta I_N$ ) for all visible and near infrared bands can be expressed as a linear function of the intensities  $I$  (Barker et al., 1983). Thus,  $I/\Delta I_N = A + BI$  where the  $A$  and  $B$  (system gain and offset, respectively) are known constants obtained from preflight calibration measurements. The complete expression for the uncertainty  $\Delta R$  is obtained by combining equations (1) and (13)

$$\Delta R = \frac{1}{I_2} \left\{ \frac{I_1 + I_2 R / (1 - \bar{R}_s)}{A + B[I_1 + I_2 R / (1 - \bar{R}_s)]} \right\} (1 - \bar{R}_s)^2 \quad (14)$$

Figure 15 shows the result of calculations based on equation (14) for all bands of the TM scene for the Wind River Basin. The values of  $I_1$  and  $I_2$  are derived from the data given in Figure 4 and the value of  $\bar{s}$  from a specific atmospheric model, as described earlier. The constants  $A$  and  $B$  are taken from Barker et al., 1983.



BAND	$\Delta$ OFFSET (IN LANDSAT-4 DN)	$\Delta$ GAIN
1	44	1.63
2	16	3.29
3	15	2.73
4	6	2.60
5	12	1.86
7	8	2.68

Figure 14. A gain and offset increase for Landsat-4 TM calculated from calibration results, Wind River Basin area, Wyoming.

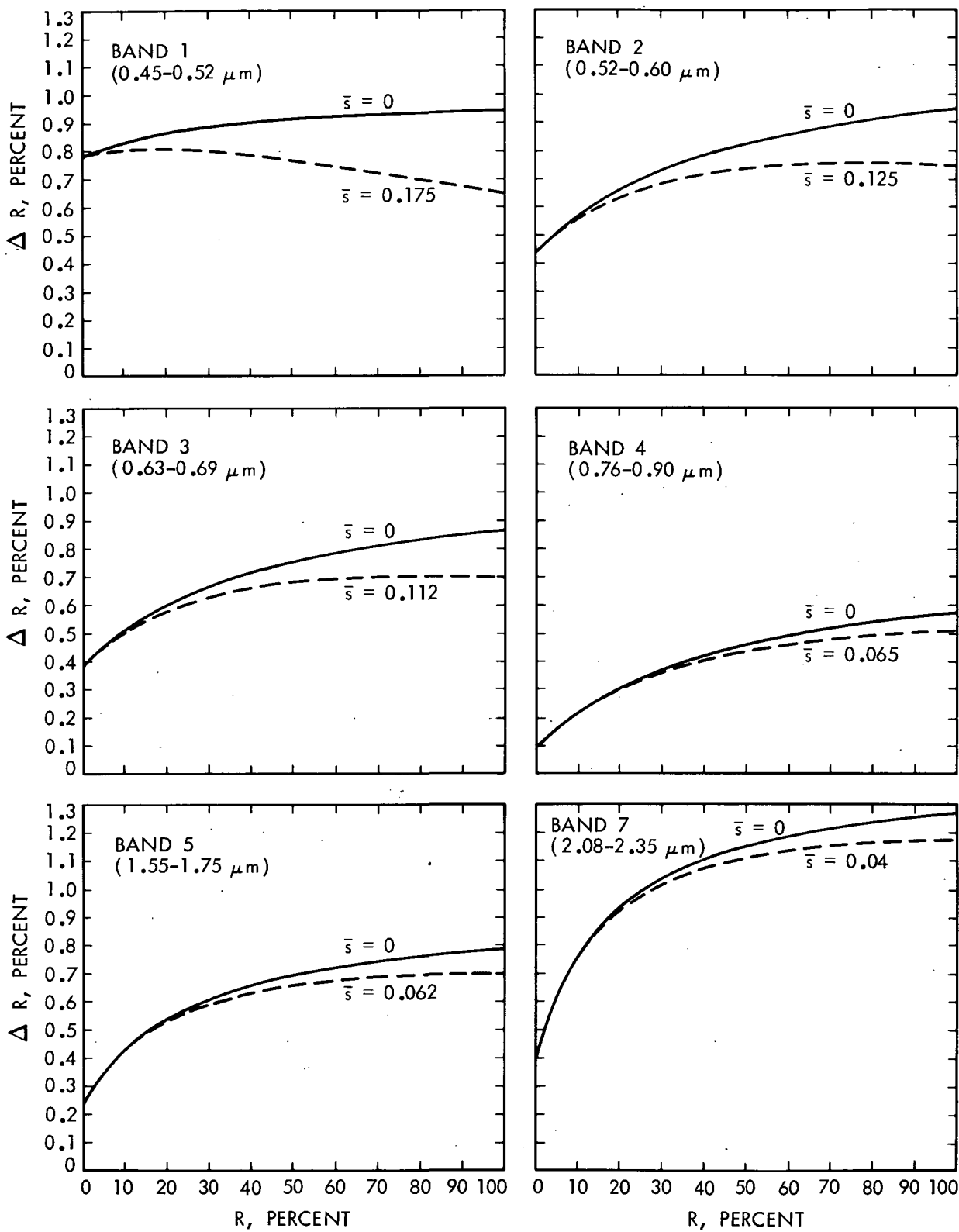


Figure 15. The reflectance uncertainty  $\Delta R$  at specific wavelengths computed as a function of surface reflectance  $R$ . Estimate of  $\Delta R$  includes both instrumental noise and effects of the atmosphere with and without  $\bar{s}$  included in the model.

Based on these calculations, the intrinsic sensitivity of the TM system to detection of changes in reflectance is less than about 1% everywhere in the scene. This conclusion is justified even for the low levels of solar illumination that characterize the Wind River TM scene.

Actual detectable reflectance differences  $\Delta R'$  are given by  $\Delta R' = 1/(dDN/dR)$ , where the derivative is obtained as the slope of a calibration line in Figure 4, and it is assumed that the minimum resolvable difference in the DN value is  $\Delta DN = 1$ . The values of  $\Delta R'$  obtained in this way for the calibration data in Figure 4 are given in Table II. It is seen that these numbers are comparable to those obtained, considering the actual signal-to-noise ratio of the TM system together with the atmospheric attenuation factors (Figure 15). On the basis of these arguments the present TM system delivers 6-bit (not 8-bit) ground reflectance information.

#### D) COMPARISON OF TM AND TMS DATA

A comparison of TM and TMS images of the Copper Mountain subarea (see Figure 16) of the Wind River Basin, Wyoming TM scene was conducted by Conel et al., (1985) and is summarized here. The subarea encompasses the Copper Mountain uranium test site, which is an area studied extensively during the NASA/Geosat Test Case Project (Abrams et al., 1985; Conel, 1983). The images were acquired at different times under different atmospheric and solar illumination conditions. A procedure using principal component transformation was employed which facilitates comparison of the two data sets. The principal components method is useful for reducing dimensionality of the data. Transformations may be computed from either the channel-to-channel covariance matrix or the correlation matrix. Principal components based on the correlation matrix represent linear transformations based on ground reflectance; thus, the separation of unique spectral classes is largely independent of non-random atmospheric and instrumental factors (Conel, 1983; Conel et al., 1985). Correlation matrix-derived principal components were used in this analysis.

Comparison of the TM and TMS correlation matrices reveals that infrared-to-visible channel correlations are lower in the TM data than in the TMS data. The difference is attributed to the presence of snow in one small area of the TM image used for comparison. Despite the minor differences in magnitude of some correlations, there is a close similarity in ranking of the two sets in order of matrix values. Similarities were quantified by computing the Spearman coefficient of rank correlation. The 0.843 coefficient indicated a 99.8% probability against TM and TMS similarities being random.

Eigenvector components were graphically compared for similarity. The first three sets of eigenvector components compare well, especially components 2 and 3. Component 4, together with components 5 and 7 are dissimilar, most likely reflecting inherent noise differences or real differences in the dispersion, possibly due to the different times of acquisition.

Table II. The quantity  $\Delta R'$  computed as the slope of lines  
in Figure 4.

Band	$\Delta R' \text{ (%)}$
1	0.65
2	1.29
3	1.09
4	1.00
5	0.65
7	1.02

TM and TMS images constructed from the first three principal components, and a geologic map of the Copper Mountain area (Thaden, 1980a and b) were also compared. It was discovered that most geologic features found in TMS data could be found in TM data as well. However, greater contrast among geologic materials in TMS as compared to TM images was apparent. This results from the differences in solar elevation ( $21^{\circ}$  for TM vs.  $55^{\circ}$  for TMS), from differences in pixel size (30 m vs. 10 m), and possibly from differences in the dynamic range between the two data sets (more dynamic range and thus more contrast for TMS data). Most stratigraphic contacts and structural features shown on the geologic map could be recognized on the images, especially the TMS data. However, several mapped formations could be subdivided on the images or extended beyond their mapped boundary. These local differences are most likely due to differences or changes in surface cover such as vegetation, soils, or eroded debris; however, some reflect errors in either mapping or image interpretations.

#### IV. GEOLOGIC APPLICATIONS

##### A) STRATIGRAPHY

The same Wind River/Bighorn Basin scene used to evaluate the Landsat-4 TM data quality was also used to investigate the stratigraphic utility of TM image data. Other reported studies of the utility of image data from these areas include Abrams et al. (1985), Conel (1983), Conel et al. (1985), Everett et al. (1983), Marrs (1978), and Parker (1974).

Reconnaissance photogeologic interpretation of the Figure 16 image at a 1:250,000 scale revealed a redbed stratigraphic unit cropping out on the margins of both the Bighorn and Wind River Basins (Figure 17). This unit provides an image-defined stratigraphic marker for regional correlation. A 1:24,000 scale stratigraphic interpretation focused on the Deadman Butte 512 x 512 TM pixel subarea (Figure 18).

Figure 19 is a color composite TM image of the Deadman Butte subarea with bands 2, 3, and 4 displayed in blue, green, and red, respectively. The image was enlarged to a 1:24,000 scale and found to match geometrically (within a few TM pixels) USGS 7-1/2' topographic maps without any rectification. Over 40 stratigraphic horizons could be mapped on the image using photogeologic methods. A simplified photogeologic interpretation of the area is shown in Figure 20. Major traceable stratigraphic horizons are numbered in ascending stratigraphic order. Topography, because of low solar elevations, is a major influence in interpretation of the image. Dips and strikes were determined using three-point solutions constrained by the image interpretations and USGS 7-1/2' topographic maps. Structures shown were defined based on dips and strikes (the syncline) and offset image horizons (the faults). No published 1:24,000 geologic maps exist for the area, but results are compatible with regional 1:500,000 and 1:250,000 scale geologic maps of the same area (Love et al., 1955 and 1978) and more detailed mapping to the west (Woodward, 1955 and 1957; Love, 1985, personal communications).

Figure 21 illustrates the same interpretation superimposed on a decorrelation stretched (Soha and Schwartz, 1978) image displaying "true-color" variations in the area (bands 1, 2, and 3 displayed in blue, green, and red). True color spectral differences are enhanced and topographic shadowing influences are suppressed (compared to Figure 20) in this version of the data.

Photogeologic interpretations of Figures 20 and 21, including dip and strike determinations, can be used with topographic information to construct the "spectral" stratigraphic column illustrated in Figure 22 (center panel). The column portrays apparent outcrop resistance, true stratigraphic thicknesses, sequence, and spectral (image color) characteristics of units identified in TM data. On the basis of known weathering characteristics, resistant units are either sandstones or carbonates and nonresistant units are shales; units that are red in tone in the bands 2, 3, and 4 version are vegetated and therefore have better soil development or higher permeability/porosity and water saturation; units that are red in the bands 1, 2, and 3 version are redbeds. These and other inferences regarding the lithologic sequence can be made directly from this spectral stratigraphic column.

ORIGINAL PAGE IS  
OF POOR QUALITY

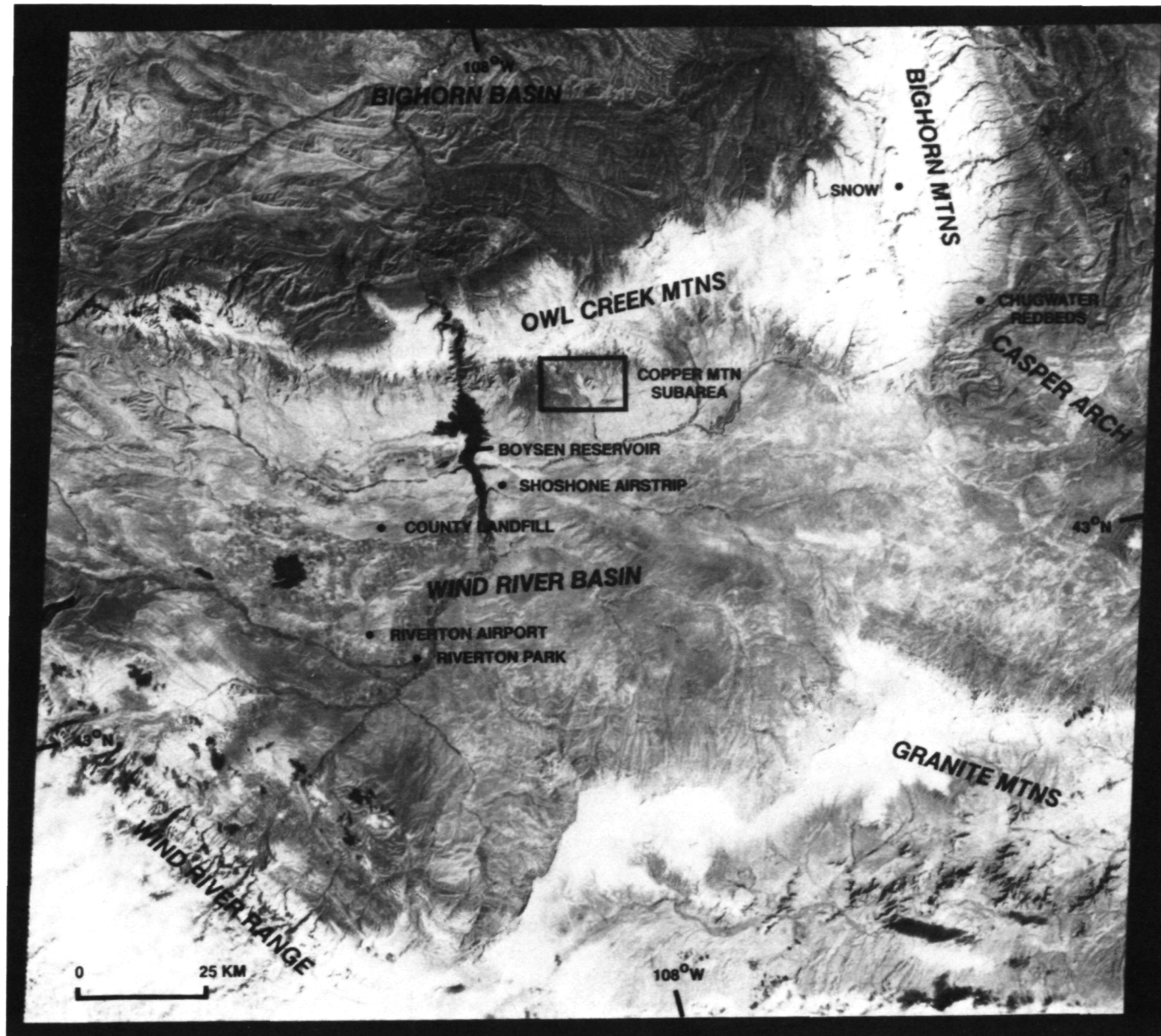


Figure 16. A full Landsat-4 scene covering a study area in central Wyoming. Bands 2, 3, and 4 are displayed in blue, green and red, respectively. Locations of the Copper Mountain test site (Conel, 1983; and Abrams et al., 1985) and field spectral sampling sites are shown. (A color slide of this figure is inserted in the plastic holder at the end of this document.)

ORIGINAL PAGE IS  
OF POOR QUALITY

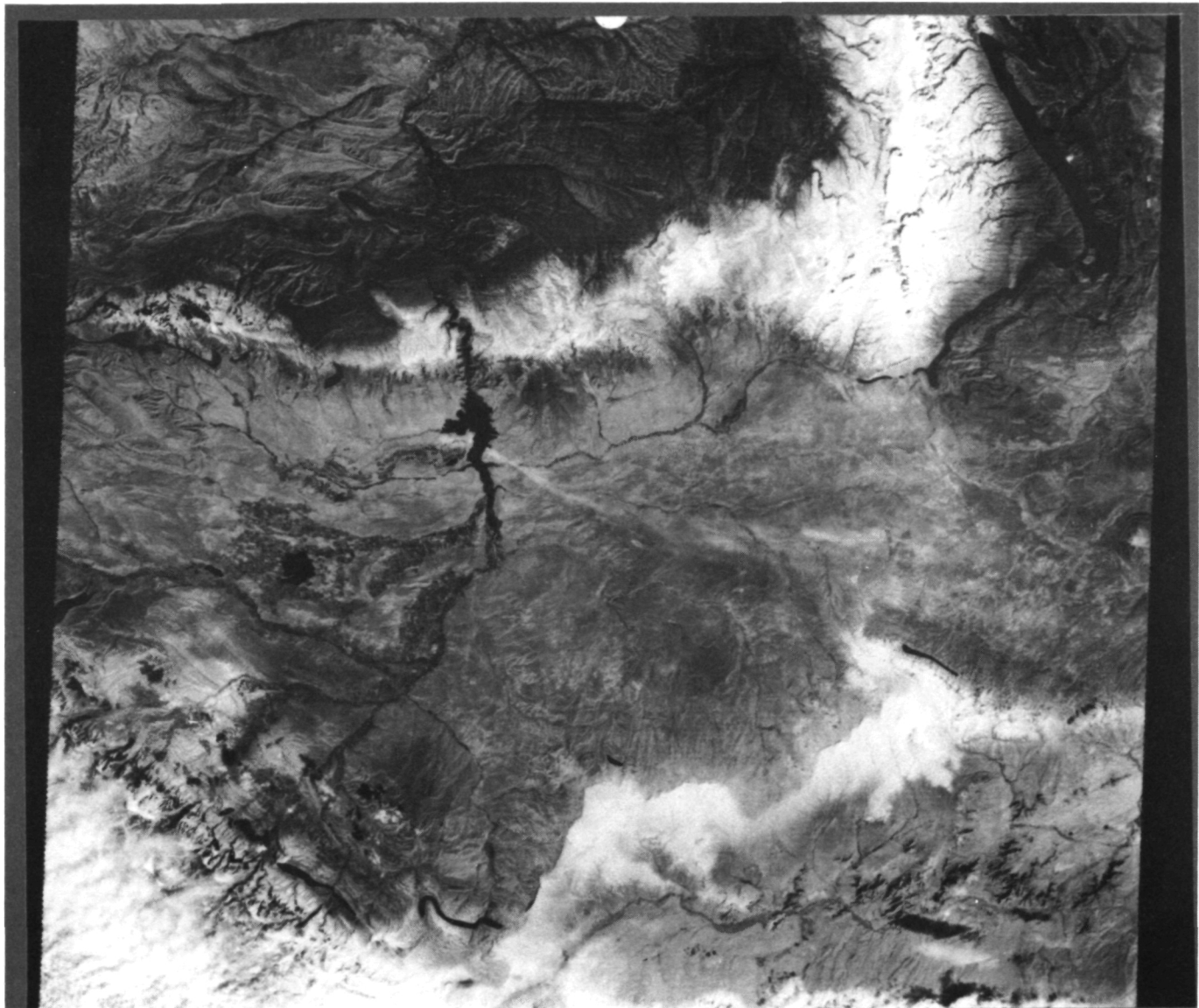


Figure 17. Same TM image as that shown in Figure 16. The distribution of a redbed stratigraphic marker is highlighted in red. (A color slide of this figure is inserted in the plastic holder at the end of this document.)

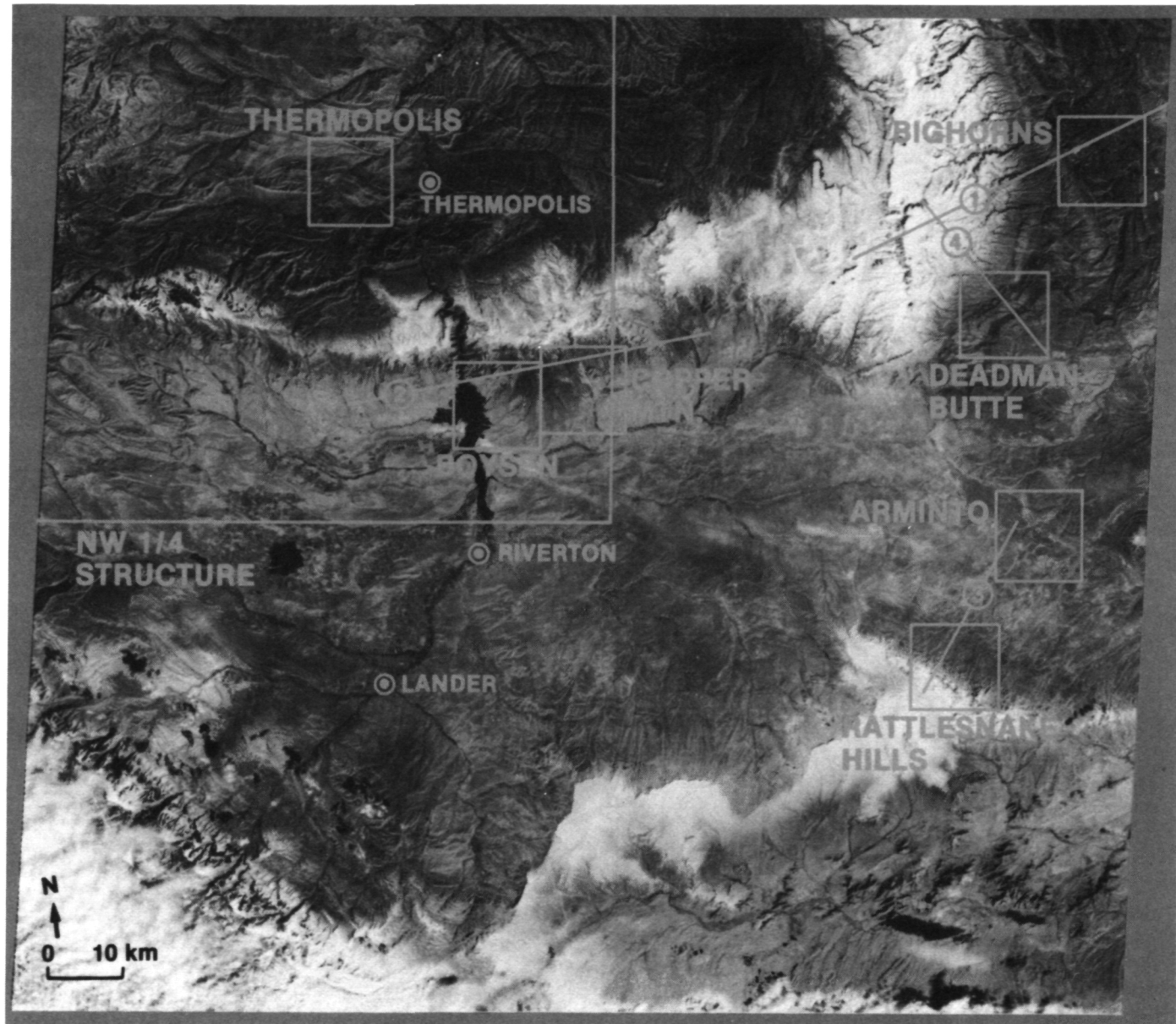


Figure 18. Landsat-4 TM color composite showing flightlines and 512 x 512 pixel subareas selected for detailed interpretation. The NW 1/4 of the scene was selected for a 1:250,000 structural interpretation. (A color slide of this figure is inserted in the plastic holder at the end of this document.)

ORIGINAL PAGE IS  
OF POOR QUALITY



Figure 19. TM bands 2 (blue), 3 (green), and 4 (red) color composite of the Deadman Butte 512 x 512 pixel subarea (see Figure 18 for location). (A color slide of this figure is inserted in the plastic holder at the end of this document.)



Figure 20. Simplified photogeologic interpretation of a TM image of Deadman Butte area (Figure 19). Also shown (dashed line) is center of flightline 4 (Figure 18). Area outlined is approximate TIMS coverage. (A color slide of this figure is inserted in the plastic holder at the end of this document.)

ORIGINAL PAGE IS  
OF POOR QUALITY



Figure 21. True color decorrelation stretch (Soha and Schwartz, 1978) bands 1 (blue), 2 (green), and 3 (red) TM image of the Deadman Butte subarea. The Figure 20 image interpretation is superimposed for comparison. (A color slide of this figure is inserted in the plastic holder at the end of this document.)

## LANDSAT-4 THEMATIC MAPPER

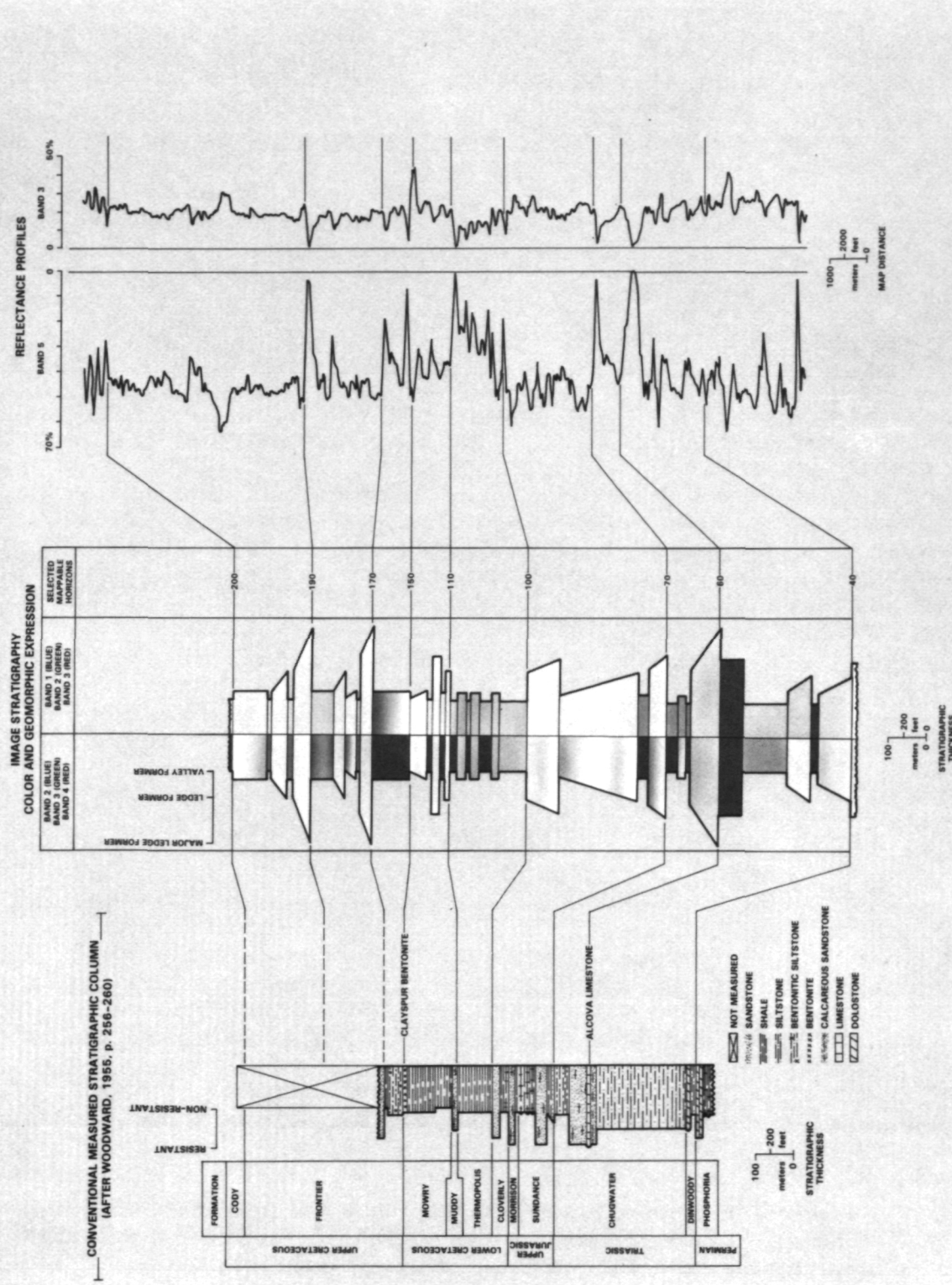


Figure 22. Comparison of a "spectral" stratigraphic column (center panel) measured along flightline 4 (Figures 20 and 21) to TM reflectance profiles (right panel) and conventional stratigraphic column (left panel). Refer to text for further explanation. (A color slide of this figure is inserted in the plastic holder at the end of this document.)

The right panel of Figure 22 portrays map-view reflectance profiles measured in TM bands 5 and 3 along the same line of section as that used to construct the spectral stratigraphic column. Stratigraphic thicknesses in this case are apparent; profiles are significantly dependent on illumination aspect, dip and strike of units, and topography. These reflectance profiles have the appearance of geophysical well logs and can indeed be used in a similar fashion for correlation purposes [Figure 23(a) and (b)]. There is, however, no necessary physical connection between such data sets.

The left panel of Figure 22 illustrates a conventional stratigraphic column measured with a Jacob's staff at a location approximately 10 km west of the Deadman Butte image area (Woodward, 1955 and 1957). Unique and complimentary aspects of the two columns are apparent. The two can be correlated. The Sundance-equivalent interval in the spectral stratigraphic column is significantly thicker than that in the conventional column. Image horizon 150 represents the Clayspur Bentonite, a regionally significant, radiometrically-dated, volcanic ashfall (McGookey, 1972). Two resistant units (sandstones?) exist (above horizon 110) in the Muddy-equivalent interval of the spectral stratigraphic column, where only one, thinner sandstone exists in the conventional column.

To demonstrate the complementary nature of TM and conventional field measurements for facies analysis, a stratigraphic panel diagram was constructed to illustrate areal thickness variability of the resistant Muddy (sandstone) Formation. Based on correlations portrayed in Figure 22, stratigraphic thicknesses of the Mowry, Muddy, and Thermopolis Formations were determined at six locations [Figure 24(b) through (g)] in the Deadman Butte TM subarea using the Figure 20 image interpretation plus topographic data. Woodward's (1957) measured section provided another location [Figure 24(a)] of known stratigraphic thickness for this interval. A stratigraphic panel diagram (Figure 25) was constructed from these data. The significant thickening of the resistant marine Muddy sandstone facies, as portrayed on the west flank of the Casper Arch, has both paleogeographic and paleotectonic significance. Image stratigraphic thickness measurements could be combined with surface and borehole measurements to construct isopachous maps of the Muddy sandstone on the Casper Arch. This information could be combined with similar mapping of the Muddy Sandstone east of the Casper Arch (Stone, 1972) to enhance our regional understanding of Early Cretaceous sedimentation and paleogeography.

## B) STRUCTURE

Previous applications of Landsat MSS data to study geologic structure have focused on reconnaissance mapping and lineament analysis. This is due mainly to inadequate spatial resolution. The TM system provides geometrically correct data with 30-meter pixels, capable of being used for more detailed structural analyses.

The structural utility of Landsat-4 TM data was evaluated with the same scene used in the stratigraphic investigation (Figure 18). A 1:24,000 scale structural analysis focused on the Thermopolis subarea illustrated in Figures 18 and 26.

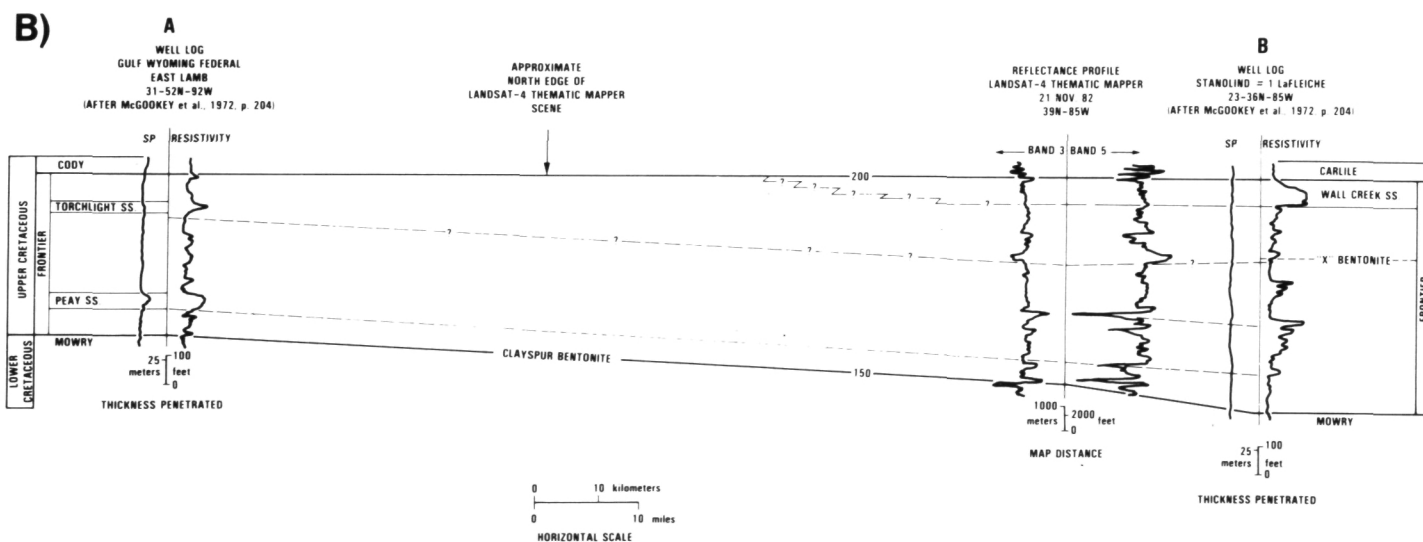
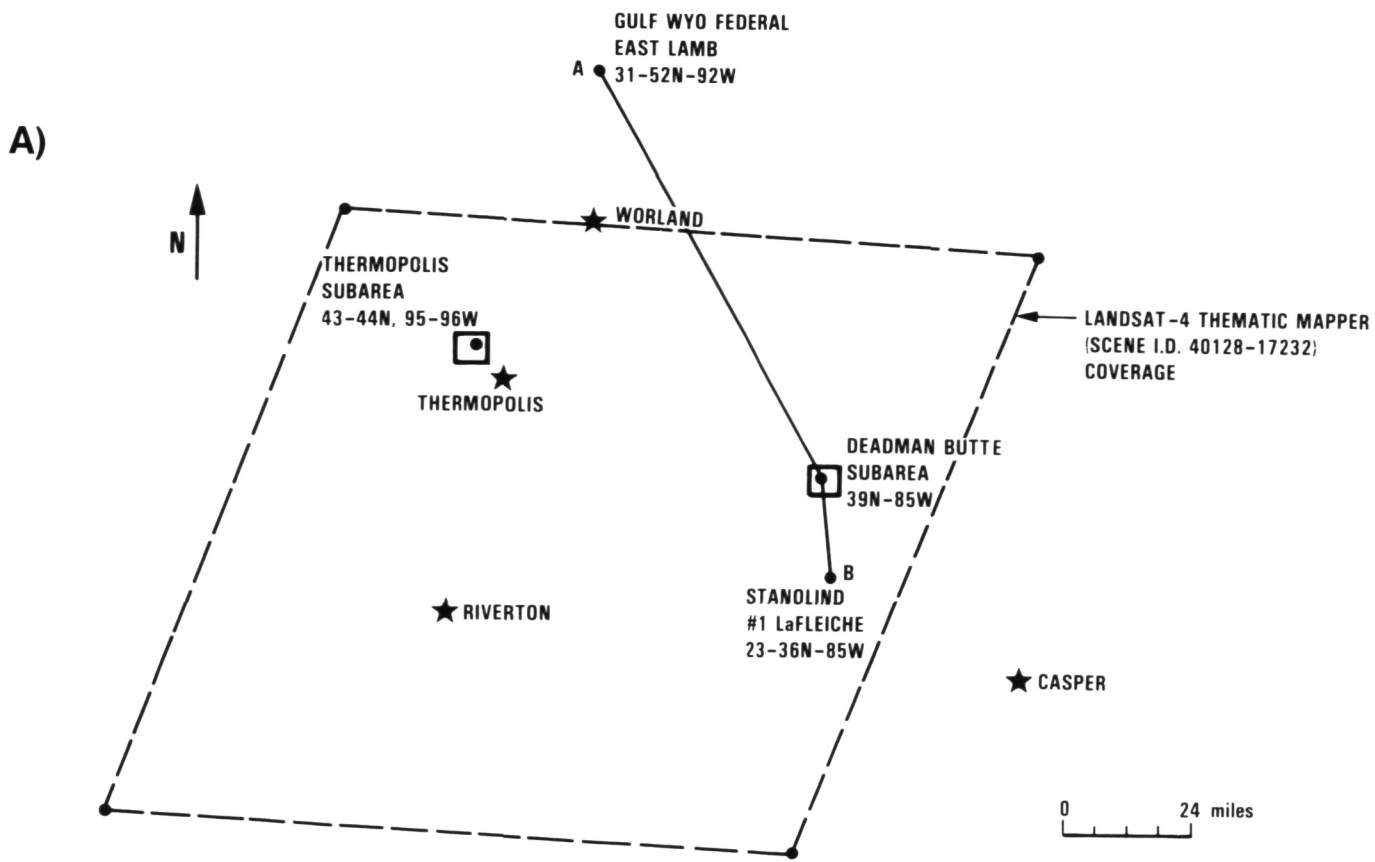


Figure 23. Stratigraphic correlation from the central Bighorn Basin (Gulf East Lamb well log), through the Deadman Butte subarea (TM reflectance profile, see Figure 22), to the central Casper Arch (Stanolind #1 La Fleiche well log): a) map showing locations of stratigraphic cross-section lines used for Figure 23(b), the outline of the Landsat-4 TM scene (Figure 18) is also shown; b) NW-SE stratigraphic cross section. Refer to Figure 23(a) for location. Image-mapping horizons 200 (datum) and 150 provide correlation horizons for integrating surface reflectance and borehole stratigraphic units (stratigraphic nomenclature and well logs from McGookey et al., 1972). In areas of low relief and known constant dip, as is the case over the Frontier interval illustrated, TM reflectance profiles can be rescaled to equivalent stratigraphic thickness. This illustrates potential compatibility of surface reflectance and borehole data for study of stratigraphic and structural problems in basin environments.

ORIGINAL PAGE IS  
OF POOR QUALITY

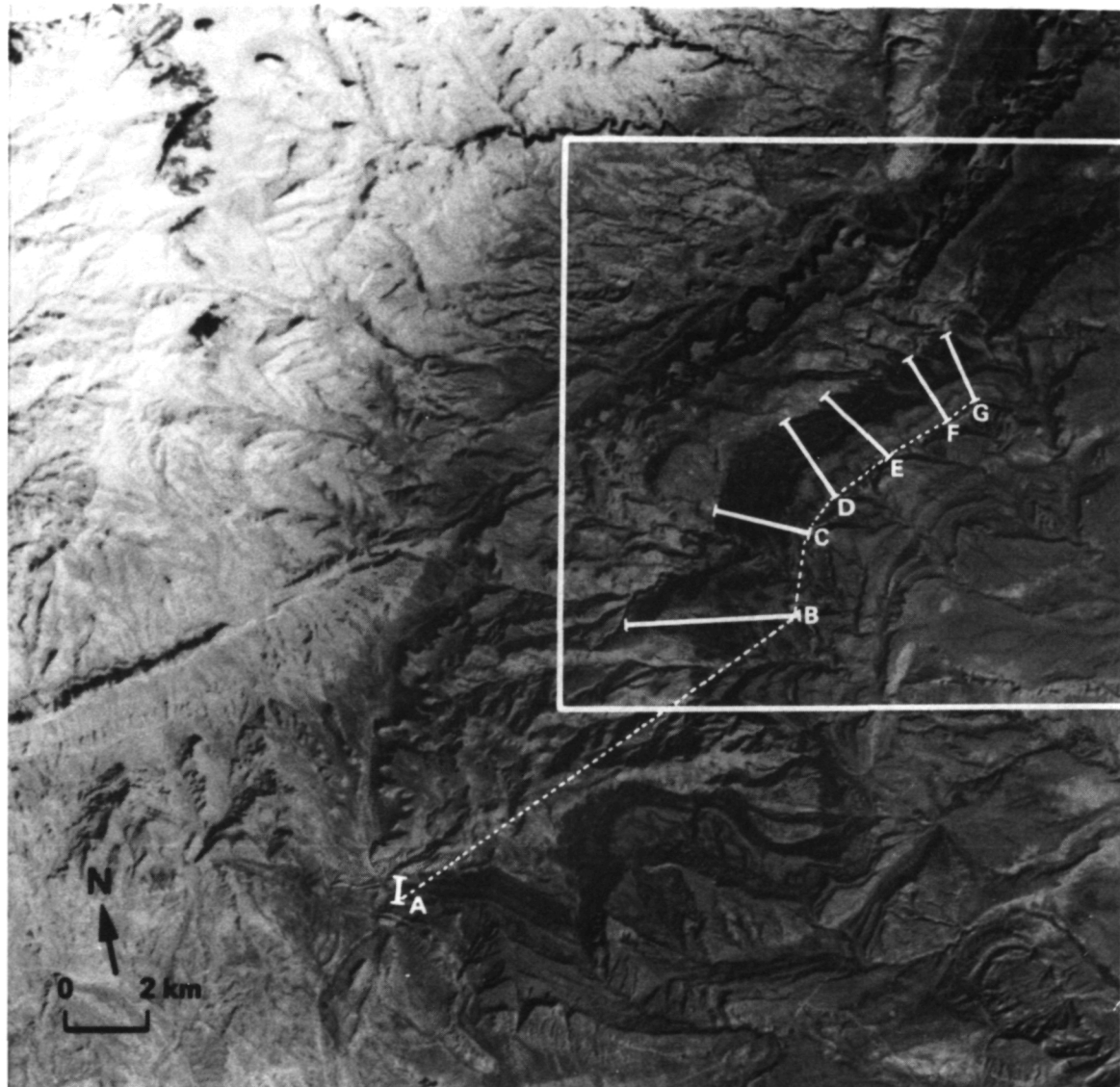


Figure 24. Landsat-4 TM bands 2 (blue), 3 (green), and 4 (red) image of the western margin of the Casper Arch showing the outline of the Deadman Butte subarea (Figure 20). Also shown are the locations of stratigraphic sections obtained from the image (b through g) and conventional (a) measurements. The location of the line of section used to construct a stratigraphic panel diagram (Figure 25) is also illustrated. (A color slide of this figure is inserted in the plastic holder at the end of this document.)

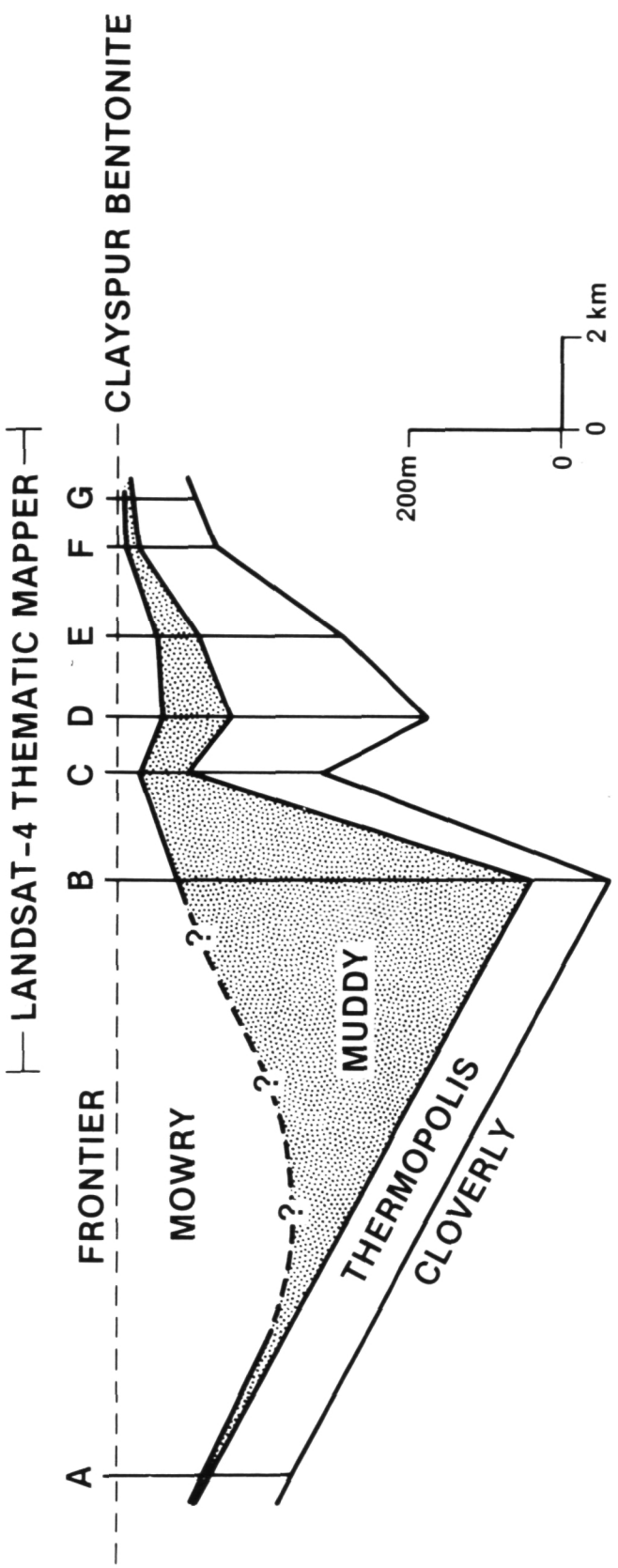


Figure 25.

Stratigraphic panel diagram illustrating a significant, previously unreported increased thickness of the Muddy sandstone facies on the west flank of the Casper Arch. (For location see Figure 24.)

ORIGINAL PAGE IS  
OF POOR QUALITY



Figure 26. TM bands 2 (blue), 3 (green), and 4 (red) color composite of the Thermopolis subarea (see Figure 18). This subarea was chosen because it contained a stratigraphic sequence equivalent to that of the Deadman Butte subarea (Figure 19) and it exhibited structural complexity. (A color slide of this figure is inserted in the plastic holder at the end of this document.)

A simplified geologic interpretation of the area is shown in Figure 27. The image is a 512 x 512 pixel, TM, color infrared composite (see Figure 26). Photointerpretations were carried out at a scale of 1:24,000 so that geologic features could be transferred directly to 7-1/2' topographic maps. No published 1:24,000 scale geologic maps exist for this area. Strike and dip measurements were determined using the 3-point procedure described for stratigraphic analysis. The red numbers on Figure 27 represent field-acquired strike and dip measurements and demonstrate that the image-derived values are accurate to approximately  $\pm 5^\circ$  dip and  $\pm 2^\circ$  strike. Dips greater than about  $60^\circ$ , however, could not be measured accurately with TM data.

The center panel of Figure 28 represents a TM-derived stratigraphic column for the Thermopolis subarea. The column was constructed along line A-A' (Figure 27) and was correlated with the Deadman Butte subarea stratigraphic column (Figure 22 and the right panel of Figure 28). As illustrated in Figure 28, more stratigraphic units are recognized in the Thermopolis subarea. This is due mainly to the illumination aspect -- bedding slopes are illuminated at Thermopolis as opposed to dip slopes at Deadman Butte.

Two significant geologic structures are apparent in the Figure 27 photointerpretations:

- 1) a northwest plunging asymmetric anticline that has vertical to overturned beds on its steeper dipping southwest limb. The axial trace of the anticline can be mapped for a total distance of approximately 40 km.
- 2) a thrust fault that cuts the southwest flank of the fold. This fault can be mapped for the entire length of the anticline. Existing geologic maps of this area do not identify this thrust fault (Love et al., 1979), or show it with normal displacement.

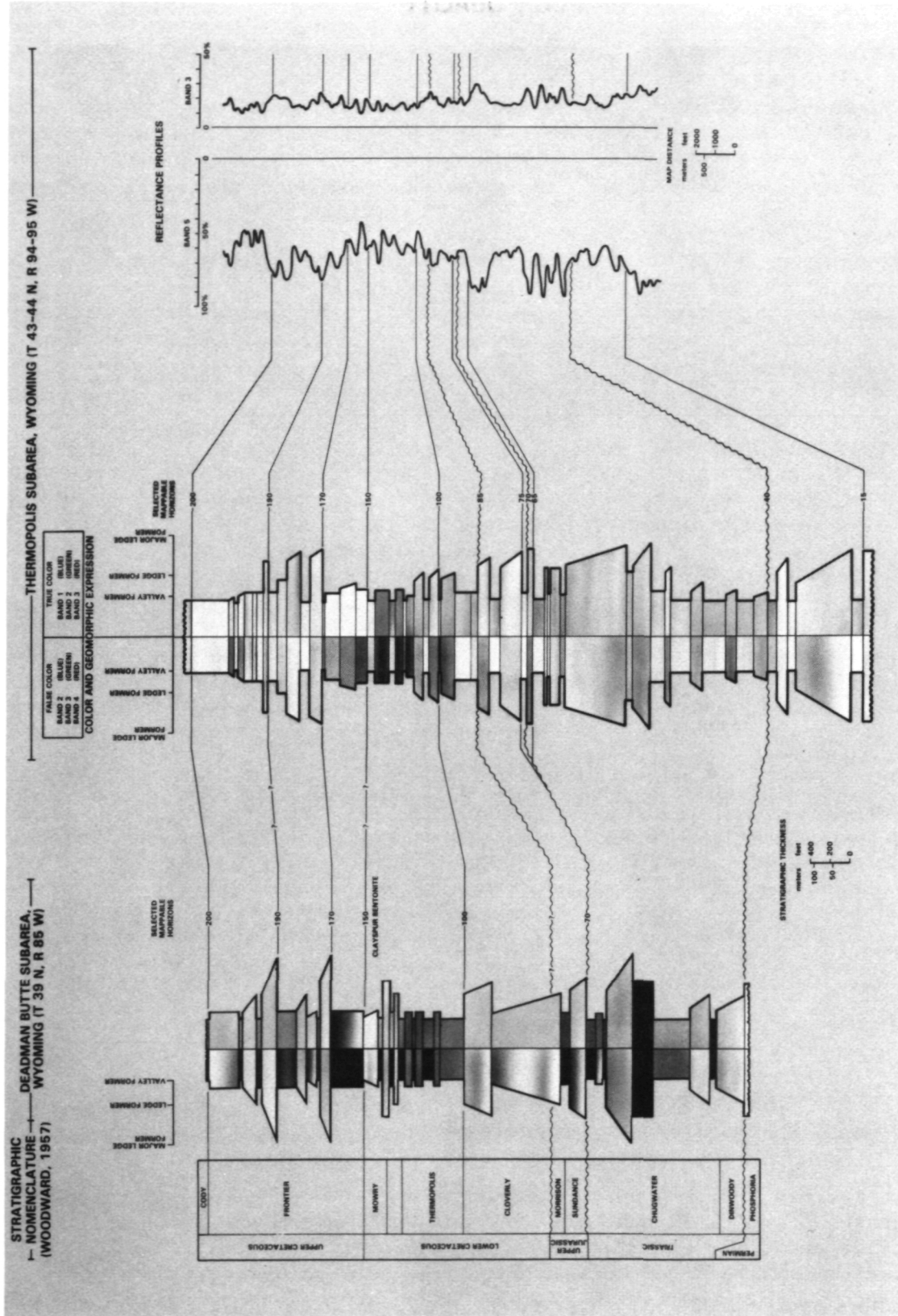
As summarized by Sales (1983) and Stone (1984), for decades geologists have debated about the geometry and mechanics of deformation of these Rocky Mountain Foreland structures. Are they high-angle, fault-induced folds (drape folds) resulting from dominantly vertical movements (e.g., Stearns, 1975)? Are they fold-thrusts resulting from dominantly horizontal movements, crustal compression, and shortening (e.g., Berg, 1962; Blackstone, 1963; Gries, 1983; and Brown, 1984)? The TM interpretation suggests that low-angle thrusts exist in this area and it supports a compressional thrust fault-fold model for deformation. Regional 1:250,000 structural interpretation of the NW 1/4 of the TM scene (Figure 18) reveals that thrust fault-folds similar to the Thermopolis structure are typical of the southern Bighorn Basin and perhaps the northwestern Wind River Basin as well.

To further illustrate these structural-style relationships, 3 cross sections were constructed using 1:24,000 enlargements of TM data, the geologic interpretation derived from the TM data, and topographic data only (Figure 29). The cross sections have a 1-to-1 aspect ratio, i.e., no vertical exaggeration. Dips and strikes of stratigraphic units were determined using the 3-point procedure. Each cross section of Figure 29 represents a different structural model of Rocky Mountain Foreland deformation: a) Stearns (1975), drape fold model; b) Berg (1962), fold-thrust model; and c) Blackstone (1963), thrust model.

ORIGINAL PAGE IS  
OF POOR QUALITY



Figure 27. Generalized photogeologic interpretation of the Thermopolis subarea (Figures 18 and 26). Red numbers represent actual strike and dip readings measured in the field for verification of image derived measurements. (A color slide of this figure is inserted in the plastic holder at the end of this document.)



Correlation of two TM spectral stratigraphic columns. Center panel illustrates the stratigraphic column for the Thermopolis subarea (refer to Figure 22 and the text for column development techniques). The left panel represents spectral stratigraphic units of the Deadman Butte subarea (Figures 18 through 22). Considerably more stratigraphic detail is expressed in the Thermopolis subarea, probably due to the illumination aspect (i.e., bedding-slope illumination as opposed to dip-slope illumination at Deadman Butte). This example clearly demonstrates that spectral stratigraphic units can be correlated from area to area, or as in this case, from basin to basin. (A color slide of this figure is inserted in the plastic holder at the end of this document.)

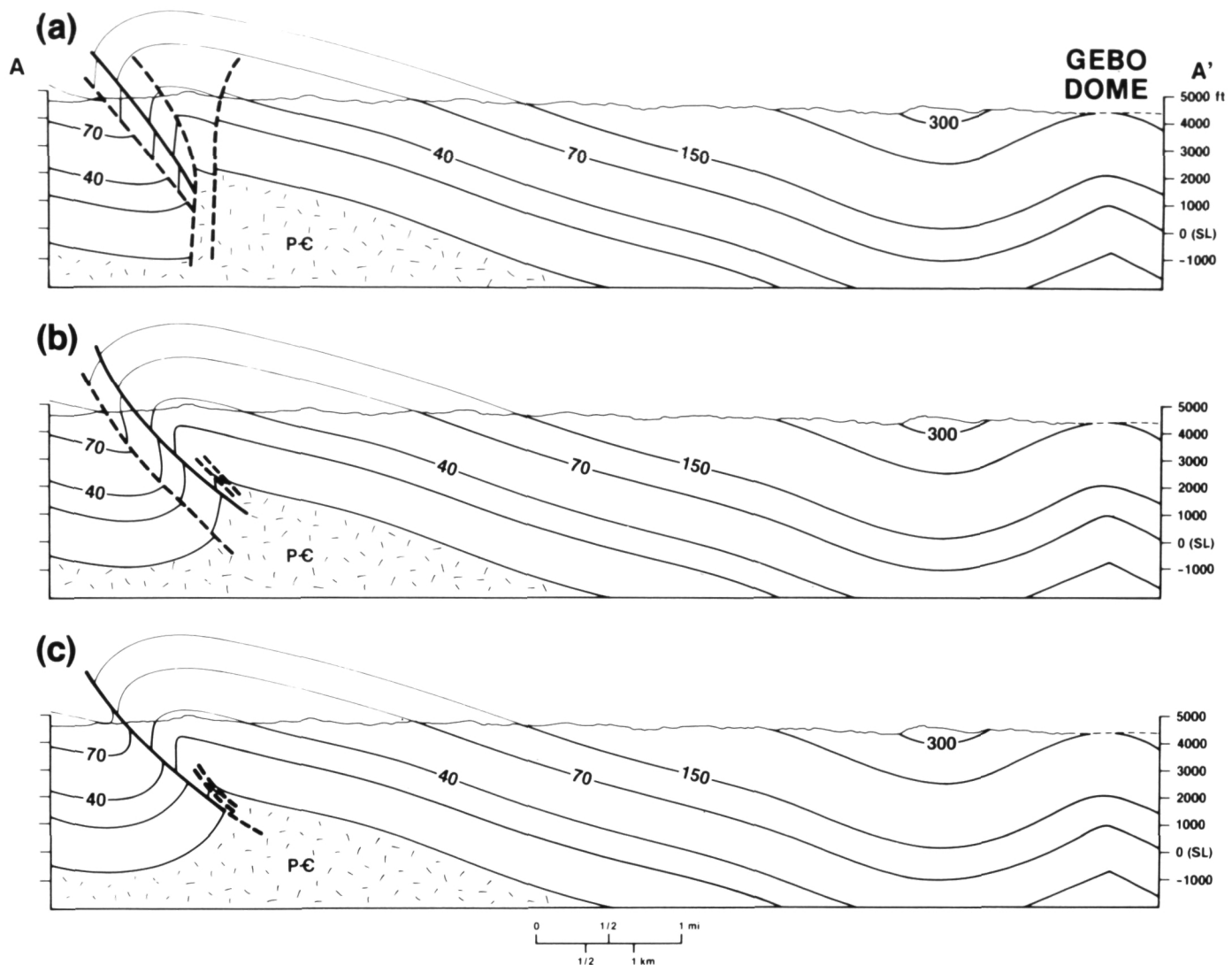


Figure 29. NE-SW trending TM-derived structural cross sections of the Thermopolis anticline. The dashed line in Figure 27 locates the line of section. Each cross section represents a different structural model that was applied to the Thermopolis Anticline in order to characterize the structure: a) Drape Fold model (Stearns, 1975); b) Fold-Thrust model (Berg, 1962); and c) Thrust model (Blackstone, 1963). The drape fold model produces an imbalanced cross section. Volumetric and bed-length conservation are only obtainable in (b) and (c). The dashed lines represent inferred faults needed to satisfy the model, but are not apparent on the image or in the field. Numbered stratigraphic horizons correspond to the stratigraphic column in Figure 28.

As described by Dahlstrom (1969), a way to verify the geometric validity of structural cross sections is to check for "structural balance." The thickness of each stratigraphic unit should remain constant throughout deformation assuming that 1) the law of conservation of volume holds true during tectonic deformation, 2) all detachment surfaces are identified, 3) the attenuation of stratigraphic units is minimal, and 4) the deformation was concentric. Thus, the surface area of a bed and its length in a cross-sectional plane must also remain constant. Given these conditions, the geometric validity of a cross section can be tested by measuring the length of several stratigraphic horizons between reference points (Dahlstrom, 1969). The length of each bed must be constant unless an intervening discontinuity (such as a decollement) exists. This method was used in constructing the cross sections in Figure 29.

Figure 29 clearly demonstrates that only cross sections or structural models incorporating thrust faults (flattening with depth) can be used to explain the geometry of the Thermopolis anticline. Bed-length conservation cannot be achieved when applying the drape fold model unless large void areas are created at the sedimentary rock/Precambrian basement interface. In Figure 29(a) approximately 13% more bed lengths, as compared to the length of the basement surface, are needed in the cross section. Structural balance can only be obtained in Figure 29(b) and (c) where the basement surface is only about 1 to 2% shorter than the overlying stratigraphic units. The dashed lines in Figure 29(a), (b), and (c) are inferred faults that are required to constrain the models, but which have not been seen on the image or in the field. Therefore, based on the balanced cross sections constrained by the TM structural interpretation and topographic data, the thrust fault model [Figure 29(c)] does the best job of representing the geometry of the Thermopolis anticline.

Figure 30 incorporates available well-log data for additional subsurface control on the interpretation. The TM-derived cross section is consistent with the well-log data. Unfortunately, no well data are available to constrain the steep southwest limb of the anticline in cross section.

These results demonstrate that TM data are useful for more detailed stratigraphic and structural analyses than were possible with MSS data. The increased spatial resolution, 1:24,000 scale enlargement capability, and good geometric fidelity allow for accurate photogeologic interpretations, including the measurement of bedding and structural attitudes. Thus, stratigraphic columns, cross sections, down plunge projections, and stereographic projections can be constrained using TM and topographic data. TM data can therefore complement conventional methods of detailed geologic studies in sedimentary basins.

### C) ALTERATION DETECTION

During this project, Landsat-4 TM data were acquired over a porphyry copper deposit at Silver Bell, Arizona that was studied using TMS data during the NASA/Geosat Test Case Project (Abrams et al., 1985). These data allowed a comparison to be made between the TMS data and the Landsat-4 TM data (Abrams, 1984).

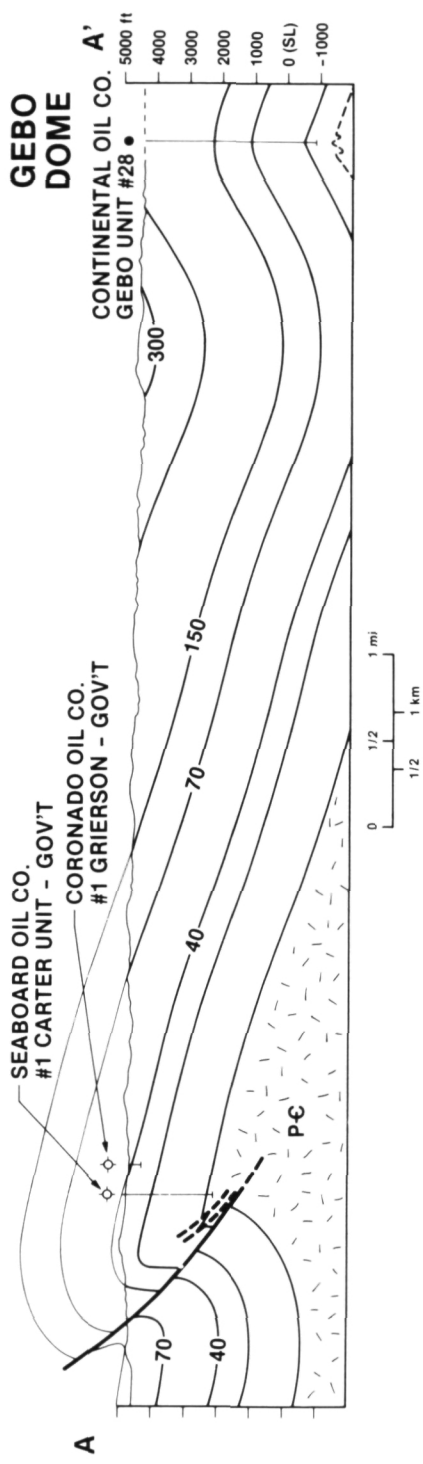


Figure 30. TM-derived structural cross section of the Thermopolis Anticline. Dashed lines on Figure 27 locate the line of section. Available well logs along the line of section are added for subsurface control. Numbered stratigraphic horizons correspond to the stratigraphic column in Figure 28.

The Silver Bell porphyry copper deposit is located in southern Arizona, 50 km northwest of Tucson. Copper, molybdenum, and silver ores are extracted from two large open pit mines. The geologic history of the area has been influenced by the west-northwest trending Silver Bell Fault Zone, which has served to localize the intrusion of shallow-level stocks and sills into country rocks consisting of carbonates, volcanic, and older intrusive rocks. Ore formation accompanied hydrothermal alteration of the dacite, alaskite, and monzonite host rocks. These have been altered to mineral assemblages dominated by hydroxyl-bearing minerals (such as kaolinite, sericite, and white mica), pyrite, and iron-oxide/hydroxide minerals. Iron-oxide minerals have diagnostic absorption bands in the 0.45 and 0.85  $\mu\text{m}$  regions of the spectrum and the hydrous minerals are characterized by absorption bands in the 2.2  $\mu\text{m}$  region and higher reflectance near 1.6  $\mu\text{m}$  (Hunt, 1977). These features make the presence of these minerals discernible using the TM spectral bands (Figure 1).

TMS data were resampled from 12-m to 30-m pixels. A color ratio composite, consisting of band ratios 6/7, 3/2, and 4/6 displayed as red, green, and blue, respectively, was produced to highlight the presence of minerals associated with alteration (Figure 31). Areas containing iron oxides are displayed in green, areas with hydrous minerals (and vegetation in the stream beds) in red, and where both occur, a yellow image color results. Superposed on Figure 31 is the outline of the phyllitic alteration zone (intense alteration with clays, sericite, and pyrite) as provided in company maps. The correspondence with the altered zone depicted on the image is excellent.

A 12-by-15 km subarea was extracted from the Landsat-4 TM scene 40128-17263, acquired November 11, 1982. A color ratio composite using the same components as the simulator image was produced from the TM data. While the alteration zone was similarly displayed, the presence of periodic horizontal striping due to residual detector miscalibrations in the TM data produced an objectionable image. Therefore, an alternate processing scheme was used.

The data were processed using a decorrelation stretch (Soha and Schwartz, 1978), which is based upon a principal component transformation. The uncorrelated data are subsequently stretched to equalize the variance and the inverse transformation is applied to return to the original coordinate space. The effect of this algorithm is to greatly exaggerate color saturation and intensity, while preserving hue information. Figure 32 is a color additive composite of TM bands 7, 5, and 1, displayed as red, green, and blue, respectively, after decorrelation stretching. (Note that horizontal striping is still evident in the image.)

In the resulting image, the alteration zone (Area A) is displayed in bright green due to the high reflectance of altered rocks in the 1.6  $\mu\text{m}$  region. A smaller green zone (K) in the Precambrian rocks to the north is also altered. The limestones (C) in the altered zone have been converted to skarn, and appear different from the unaltered limestones at (N). In addition to the discrimination of altered rocks, various other rock types are separable on the image based on color differences (Table III).

ORIGINAL PAGE IS  
OF POOR QUALITY

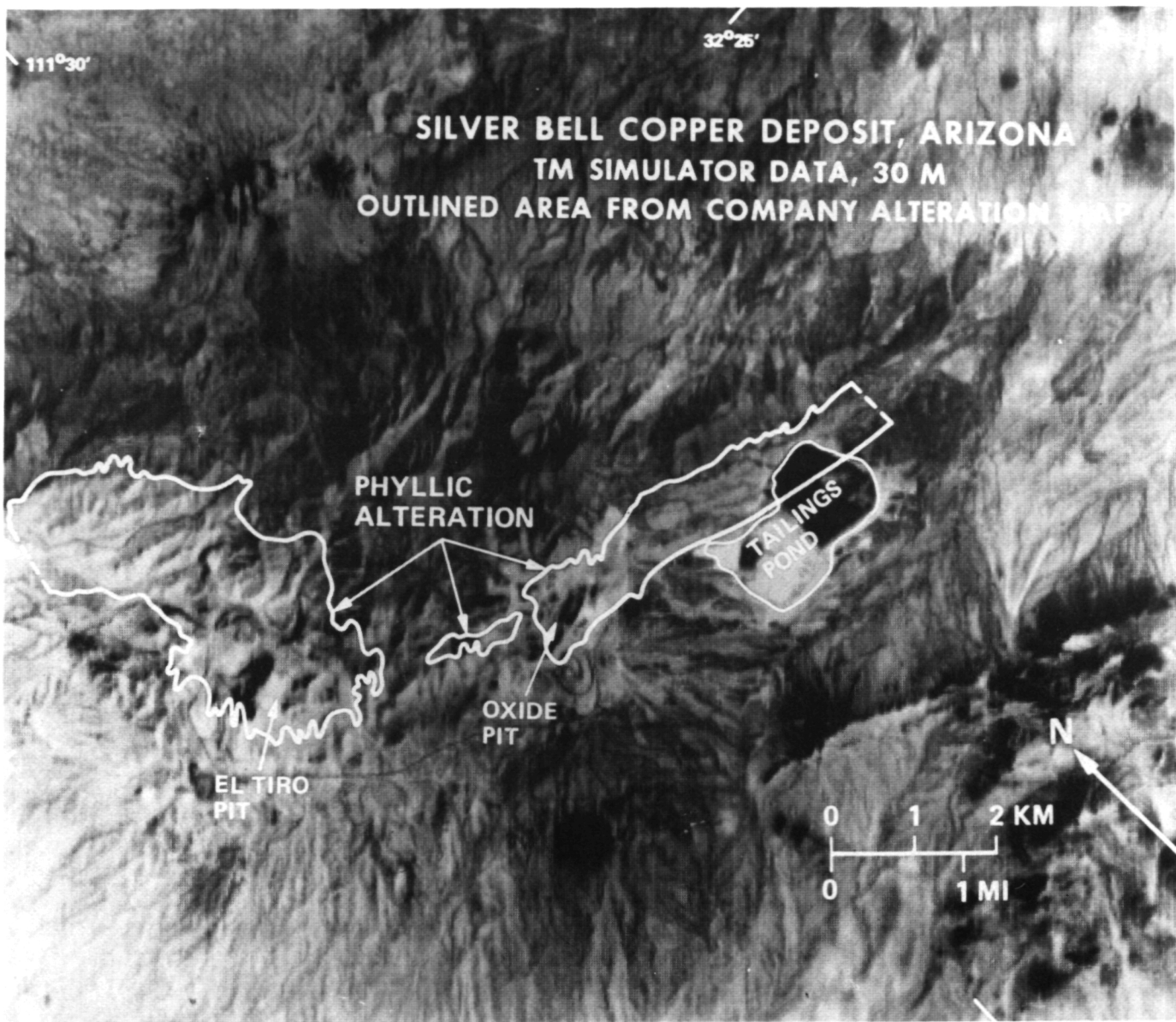


Figure 31. TMS data over the Silver Bell copper deposit, Arizona, resampled to 30-m pixels. Band ratios  $1.65/2.2 \mu\text{m}$ ,  $0.66/0.56 \mu\text{m}$ , and  $0.83/1.65 \mu\text{m}$  are displayed as red, green, and blue, respectively. The main alteration zone is displayed in yellow due to the presence of hydroxyl-bearing minerals and iron-oxide minerals. The phyllitic alteration zone mapped from field and laboratory data is superimposed for comparison. (A color slide of this figure is inserted in the plastic holder at the end of this document.)

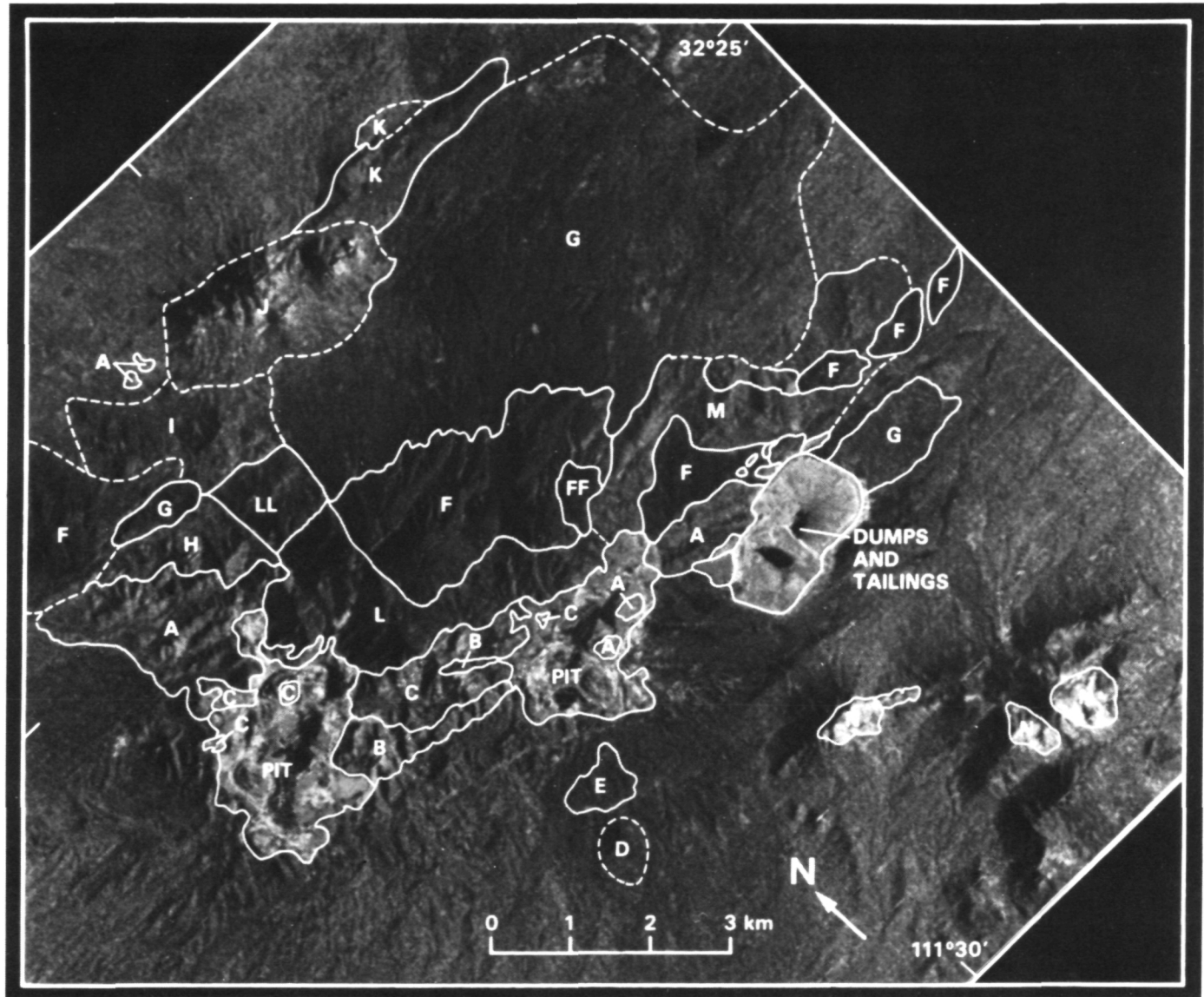


Figure 32. Landsat-4 TM data over the Silver Bell copper deposit, Arizona. Bands 7, 5, and 1 are displayed as red, green, and blue, respectively. The main alteration zone is displayed in green due to the high reflectance of hydrous minerals in the  $1.65 \mu\text{m}$  region (band 5). Letter units are identified in Table III (scene 40128-17263, acquired November 11, 1982). (A color slide of this figure is inserted in the plastic holder at the end of this document.)

Table III. Key to symbols on Figure 32

Symbol	Description
A	Phyllitic alteration
B	Altered monzonite
C	Limestone
D	Basalt
E	Redbeds
F, FF	Mt. Lord Ignimbrites
G	Silver Bell andesite, mudflows
H	Claflin Ranch agglomerate
I	Granodiorite
J	Ragged Top latite
K	Precambrian schist/granite
L, LL	Dacite
M	Mixed intrusives
N	Limestone

The Landsat-4 TM data allow identification of hydrothermal alteration zones in arid regions, based on detection of spectral features associated with hydroxyl-bearing and iron-oxide minerals. It is the position of the spectral bands, rather than the particular image processing algorithm applied, that allows this identification to be made, thus confirming the results of the previous TMS data analysis.

#### D) LITHOLOGIC MAPPING

Preliminary analyses were performed on Landsat-4 TM scene 40124-17495, covering Death Valley, California, and were obtained in P-tape format. A geologic map of the area is shown in Figure 33 for comparison with images.

In order to examine the utility of the TM data at fully useable spatial resolution, several small areas were extracted from the TM scene for image processing. A 27-by-18 km area covering the east side of the Panamint Mountains, alluvial fans descending to the valley floor, part of the Death Valley salt pan, and Trail Canyon was examined (Figure 34). Data were processed using band ratioing, color-enhanced band composites, and principal component transformations. The principal component image is shown in Figure 34. Lithologic interpretation maps were prepared and compared to published geologic maps of the area at a scale of 1:62,500. More detailed, delineation of alluvial fan units were evident on the TM images compared to published maps. The oldest fans had dendritic drainage patterns developed on their surfaces, while younger fans were characterized by the presence of parallel-to-braided drainage patterns. The 30-m pixel size was more than sufficient to resolve these drainage features. Spectral contrast between fans was related to differences in source rock composition and variable development of weathering and varnish surfaces. All mapped fan units were separable based on geomorphic characteristics. Additional units were identified based on spectral differences. Of the three different enhancement procedures used, ratioing produced the least useful images due to exaggeration of noise and artifacts.

A second area, 15 by 15 km over the Tucki Mountains, at the northwest end of Death Valley, was extracted from the TM scene to examine the utility of the data for separating sedimentary rock types. Quartzites, shales, dolomites, limestones, and sandstones, dipping 50 to 90 degrees are exposed in the Tucki Mountains. Topographic relief is rather severe; however, exposures are excellent because vegetation cover is minimal to absent. Again the principal component composites and enhanced band composites were the most satisfactory for display of the data. Many of the mapped rock types were separable based on spectral differences. Problems occurred along north-facing slopes due to deep shadows resulting from the low sun angle during the November data acquisition; no lithologic boundaries were discernible in these shadowed areas.

The same two areas were extracted from Landsat-2 MSS data for comparison to the TM data. The improvement in spatial resolution of the TM was apparent. No details of drainage patterns on the fans were visible on the MSS data, making geomorphic interpretations impossible. In addition, the limited spectral coverage of MSS data reduced the amount of lithologic separations displayed on the images.

ORIGINAL PAGE IS  
OF POOR QUALITY



Figure 33. Geologic map of the Death Valley area from Hunt and Mabey (1966). Bedrock units to the left side of the map consist of Precambrian to Ordovician dolostones, with some shales, quartzites, limestones, and Tertiary volcanic rocks such as rhyolitic tuffs and basalts. Four alluvial fan units (yellow) are identified by Hunt and Mabey, based upon relative weathering and geomorphic characteristics. The valley fill (gray), on the right center of the map, consists of carbonate and sulfate salts, intermixed with argillaceous materials, gypsum, caliche, and borate salts. (A color slide of this figure is inserted in the plastic holder at the end of this document.)

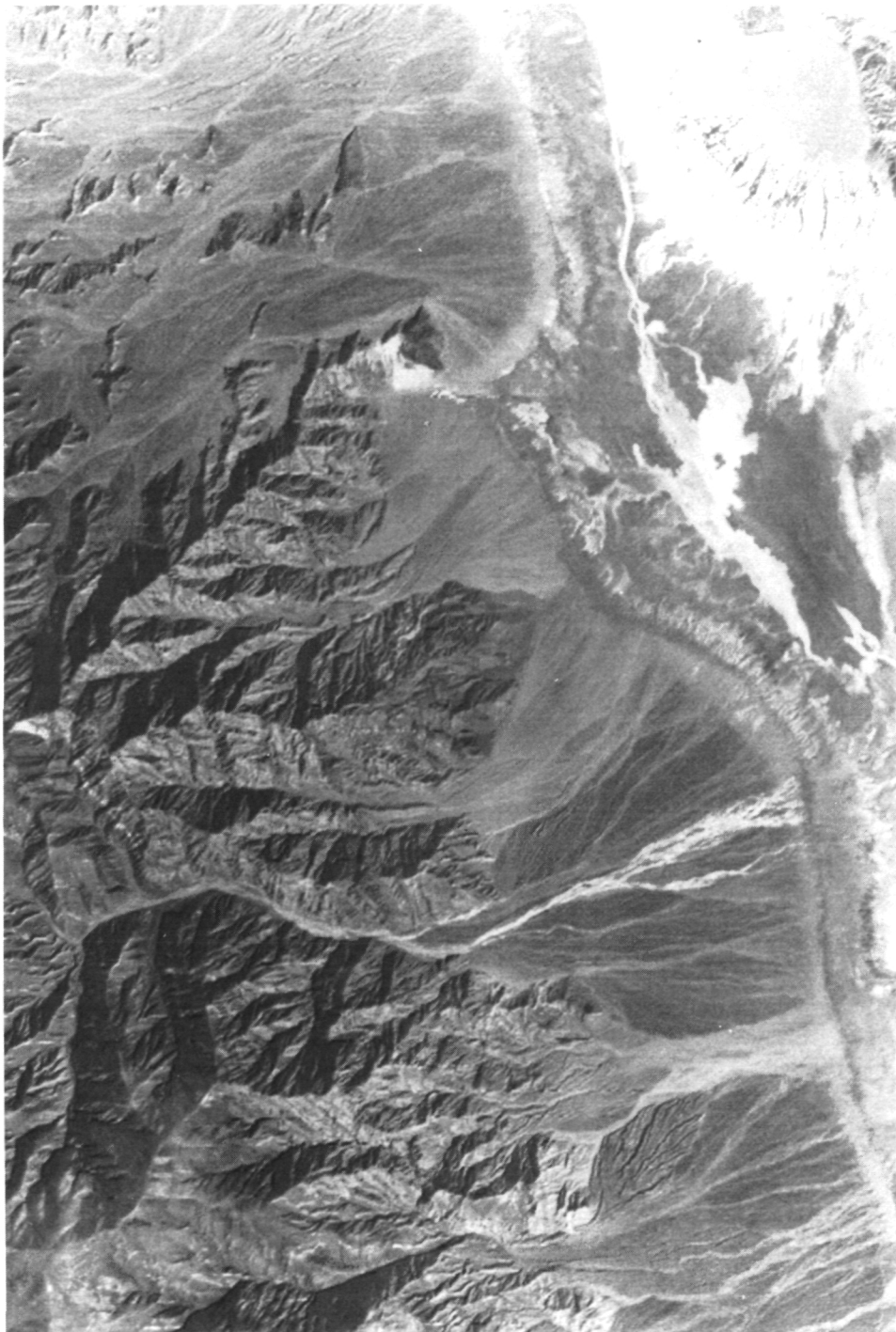


Figure 34. Landsat-TM principal component image of part of the Death Valley area. Components 1, 2, and 3 are displayed in red, green, and blue, respectively. The Furnace Creek fan is located in the upper right-hand corner of the image. The Trail Canyon fan is located slightly below the center of the image. (A color slide of this figure is inserted in the plastic holder at the end of this document.)

A larger area (40 by 60 km) was processed to examine the effects of using different spectral channels in false-color composites. The data were processed using decorrelation stretching (Soha and Schwartz, 1978) and combined in various triplets to produce a color composite. The most useful combination examined was created using TM bands 4, 5, and 7 -- the three infrared bands. This is expected because major spectral contrast between different rock types occurs in the infrared part of the spectrum. This points out one advantage of TM over MSS data -- the presence of two channels beyond 1  $\mu\text{m}$ .

The TM data were digitally registered to a topographic base map, then Seasat radar data and six channels of multispectral thermal aircraft data (TIMS) (8.2 to 12.2  $\mu\text{m}$  range) were registered to this data base. The objective was to assess the improvement in material separation possible using this multisensor data set. Each data set measures a different surface physical property: the TM is sensitive to reflectance characteristics which are mainly controlled by the presence of iron, water, hydroxyl ion, and carbonate ion, and overall brightness or albedo; the TIMS is sensitive to the presence of free silica, hydroxyl ion, density, albedo, and conductivity; the Seasat radar is sensitive to surface roughness, slope, water content, and orientation.

A principal component transformation was applied using 13 input variables: six TM bands excluding thermal, six thermal multispectral scanner bands, and one Seasat band. Composites were created using various triplets of the eigenpictures, and two were selected for mapping of fan and rock units, one of which is shown in Figure 35 (components 2, 3, and 4 are displayed in blue, green, and red, respectively). Based on visual inspection and mapping results, both composites had more information displayed using the combined data set than was apparent in images created from any of the data sets alone. Examination of the images and the eigenvectors indicated that the contribution of the radar data was negligible. Instead, the combination of spectral data from the reflectance and emittance parts of the spectrum was responsible for the improvement in rock-type separation.

Another study was done for an area of the TM scene covering the Telescope Peak 15-minute quadrangle (Albee et al., 1984). The data corresponding to the quadrangle were extracted and analyzed at the map scale of 1:62,500. Decorrelation stretching was applied to the data, and a composite produced using channels 2, 5, and 7. This image permitted discrimination of quartzofeldspathic rocks, dolostones, limestones, granitic intrusions, and heavily weathered alluvium. Contacts mapped from the TM image agreed well with those on the published geologic map of the quadrangle.

ORIGINAL PAGE IS  
OF POOR QUALITY

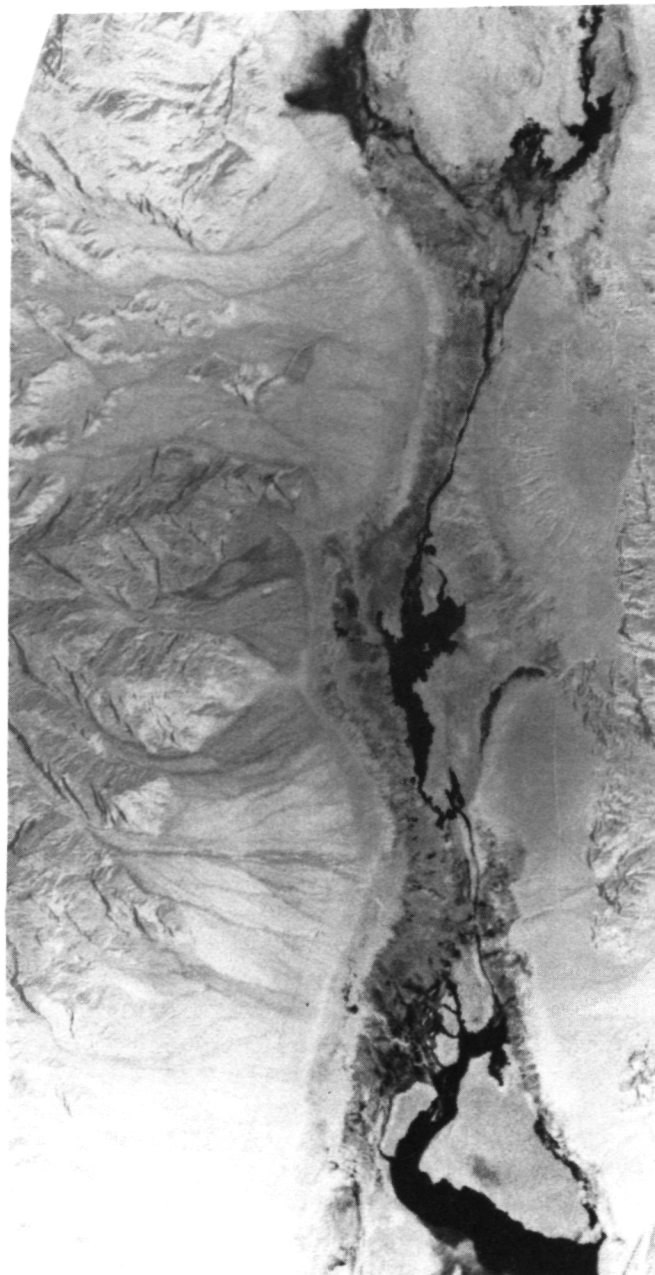


Figure 35. Principal component image of the Death Valley area using 13 input variables, including 6 TM channels, 6 TIMS channels, and a Seasat Radar image. Components 2, 3, and 4 are displayed in blue, green, and red, respectively. The area covered is approximately the same as that covered by the geologic map in Figure 33. The Furnace Creek fan is orange and is located on the right-hand side of the image. (A color slide of this figure is inserted in the plastic holder at the end of this document.)

## V. CONCLUSIONS

The Landsat-4 TM sensor is a significant improvement compared to other satellite remote sensing systems. The system provides increased spatial and spectral resolution, which are particularly useful for geologic applications. Specific conclusions of this work are as follows:

- 1) Artificial targets, one of high albedo and one of low albedo, are feasible, field-deployable standards that can be used to investigate scanner radiometry and calibration.
- 2) Large, spectrally homogeneous ground targets (natural or artificial) can be used to derive empirical/theoretical relationships between image DN and ground reflectance for atmospheric calibration of TM data, estimation of atmospheric parameters, and construction of atmospheric MTF's.
- 3) No significant radiometric degradation occurs in TM data as a result of radiometric and geometric corrections by SCRUNGE processing.
- 4) TM data exhibit narrow DN distributions (dynamic range) suggesting that the configuration of the instrument is not sufficient to utilize the available 256-DN range (8 bits); the present instrument gain and offset settings are not optimal for earth science applications.
- 5) Increased spatial resolution, 1:24,000 enlargement capability, and good geometric fidelity of TM data allow accurate photogeologic interpretations, including measurement of bedding and structural attitudes when used in conjunction with topographic data. This makes possible: a) the construction of stratigraphic columns; b) the correlation of stratigraphic units; c) the construction of stratigraphic panel diagrams; and d) the construction of structural cross sections, down plunge projections, and stereographic projections, which complement conventional methods of detailed stratigraphic and structural analysis.
- 6) TM bands 5 and 7 are particularly useful for geologic applications because they span a region of the spectrum not previously sampled with MSS data and are important for characterizing geologic surface materials such as clay and carbonate minerals.
- 7) TM data are useful for detection of iron-bearing and hydroxyl-bearing alteration zones associated with base and precious metal deposits.
- 8) A 30-m pixel size of the TM data is sufficient to resolve geomorphic characteristics of alluvial fans, allowing separation based on relative ages.

## VI. ACKNOWLEDGEMENTS

The authors would like to thank several people for their help with different aspects of this project: Helen Paley and Deborah Dunn for their assistance in editing this manuscript; Steve Adams, Ron Alley, and Stan Schultz for continuity of computer activities; Gordon Hoover for his electronic wizardry; and numerous other JPL and non-JPL people for their help in field activities and data reduction tasks.

## VII. REFERENCES CITED

- Abrams, M., 1984, Landsat-4 Thematic Mapper and Thematic Mapper Simulator data for a porphyry copper deposit: Photogrammetric Engineering and Remote Sensing, Vol. 50, p. 1171-1173.
- Abrams, M., J. E. Conel, and H. R. Lang, 1985, The Joint NASA/Geosat Test Case Project, Final Report: Am. Assoc. Petrol. Geol., Tulsa, Oklahoma, 1381 p.
- Albee, A., M. Abrams, A. R. Gillespie, and A. B. Kahle, 1984, Discrimination of lithologic units in the Panamint Mountains using spectral and multichannel image data: Abst., Geological Society of America Annual Meeting, Reno, Nevada, November 5-8, 1984.
- Barker, J. L., and F. J. Gunther, 1983, Landsat-4 sensor performance: Proceedings Pecora VIII, Satellite Land Remote Sensing, Advancements for the Eighties, Sioux Falls, South Dakota, p. 46-74.
- Barker, J. L., D. L. Ball, K. C. Leung, and J. A. Walker, 1983, Prelaunch absolute radiometric calibration of the reflective bands on Landsat-4 protolight thematic mapper: Abstracts of Landsat-4 Early Results Symposium, NASA/Goddard Space Flight Center, Greenbelt, MD, February 22-24, 1983.
- Berg, R. R., 1962, Mountain flank thrusting in the Rocky Mountain Foreland, Wyoming and Colorado: Am. Assoc. Petrol. Geol. Bull., Vol. 46, p. 2019-2032.
- Blackstone, D. L., 1963, Development of geologic structures in the Central Rocky Mountains, in Backbone of the Americas (O. E. Childs, ed.): Am. Assoc. Petrol. Geol., Memoir 2, p. 160-179.
- Brown, W. G., 1984, A reverse fault interpretation of Rattlesnake Mountain anticline, Bighorn Basin, Wyoming: The Mountain Geologist, Vol. 21, p. 31-35.
- Chandrasekhar, S., 1960, Radiative transfer: Dover Publications, Inc., New York, p. 269-274.
- Chandrasekhar, S., and D. Elbert, 1952, The X and Y functions for isotropic scattering, II: Astrophysical Journal, Vol. 115, p. 269-278.
- Conel, J. E., 1983, Interpretation of aircraft multispectral scanner images for mapping of alteration with uranium mineralization, Copper Mountain, Wyoming: International Geoscience and Remote Sensing Symposium (IGARSS '83), II, FP-6, p. 5.1-5.6.
- Conel, J. E., H. R. Lang, and E. D. Paylor, 1985, Preliminary spectral and geologic analysis of Landsat-4 Thematic Mapper data, Wind River Basin area, Wyoming: IEEE Transactions in Geoscience and Remote Sensing, Vol. GE-23, no. 4, p. 562-573.

Dahlstrom, C. D. A., 1969, Balanced cross sections: Canadian Jour. of Earth Sciences, Vol. 6, p. 743-757.

EROS (Earth Resources Observational Satellite) Data Center, 1979, Landsat Data Users Handbook: U. S. Geol. Survey, Sioux Falls, South Dakota.

Everett, J. R., J. D. Dykstra, C. A. Sheffield, 1983, Contribution of Landsat-4 Thematic Mapper data to geological exploration: Proceedings Pecora VIII, Satellite Land Remote Sensing, Advancement for the Eighties, Sioux Falls, South Dakota, p. 162-168.

Gillespie, A. R., A. B. Kahle, and F. D. Palluconi, 1984, Mapping alluvial fans in Death Valley, California, using multichannel thermal infrared images: Geophysical Research Letters, Vol. 11, no. 11, p. 1153-1156.

Goddard Space Flight Center, 1982, Landsat-D Investigations Workshop: Report of the Landsat-D investigators workshop held at Goddard Space Flight Center, Greenbelt, Maryland, May 13-14, 1982, 2 volumes.

Goetz, A. F. H., B. N. Rock, and L. C. Rowan, 1983, Remote sensing for Exploration: An Overview: Economic Geology, Vol. 78, no. 4, p. 573-590.

Goetz, A. F. H. and L. C. Rowan, 1981, Geologic remote sensing: Science, Vol. 211, p. 781-791.

Gries, R., 1983, North-south compression of Rocky Mountain Foreland structures, in Rocky Mountain Foreland Basins and Uplifts, (D. J. Lowell, ed.): Rocky Mountain Assoc. of Geologists, p. 9-32.

Hunt, C. B. and D. R. Mabey, 1966, Stratigraphy and structure of Death Valley, California: U.S. Geol. Survey Prof. Paper 494-A, US Govt Printing Office, Washington, DC.

Hunt, G. R., 1977, Spectral signatures of particulate minerals in the visible and near infrared: Geophysics, Vol. 42, p. 501-513.

Kahle, A. B., and A. F. H. Goetz, 1983, Mineralogic information from a new airborne thermal infrared multispectral scanner: Science, Vol. 222, p. 24-27.

Kahle, A. B., J. P. Schieldge, and R. E. Alley, 1984, Sensitivity of thermal inertia calculations to variations in environmental factors: Remote Sensing of Environment, Vol. 16, no. 3, p. 211-232.

Kaufman, Y. J., 1982, Solution of the equation of radiative transfer for remote sensing over nonuniform surface reflectants: Journal of Geophysical Research, Vol. 87, C 6, p. 1437-1447.

Kaufman, Y. J., 1984, Atmospheric effects on remote sensing of surface reflectance: SPIE Remote Sensing, Vol. 475, p. 20-33.

- Kaufman, Y. J., and J. H. Joseph, 1982, Determination of surface albedos and aerosol extinction characteristics from satellite imagery: Journal of Geophysical Research, Vol. 87, C 2, p. 1287-1299.
- Love, J. D., A. C. Christiansen, J. L. Earle, and R. W. Jones, 1978, Preliminary geologic map of the Armito  $1^{\circ} \times 2^{\circ}$  quadrangle, Central Wyoming: U. S. Geol. Survey Open-File Report 78-1089.
- Love, J. D., A. C. Christiansen, T. M. Brown, and J. L. Earle, 1979, Preliminary geologic map of the Thermopolis  $1^{\circ} \times 2^{\circ}$  quadrangle, Central Wyoming: U. S. Geol. Survey Open-File Report 79-962.
- Love, J. D., J. L. Weitz, and R. K. Hose, 1955, Geologic map of Wyoming: U. S. Geol. Survey Map Series, MS-7A, 7B.
- Marrs, R. W., 1978, Geologic remote sensing in the Wind River Basin, in Resources of the Wind River Basin (R. B. Boyd, ed.): Wyoming Geological Association Guidebook, p. 47-53.
- McGookey, D. P., 1972, Cretaceous system, in Geologic Atlas of the Rocky Mountains (W. W. Mallory, ed.): Rocky Mountain Association of Geologists, Denver, p. 190-228.
- NOAA, 1983, Landsat Data Users Notes, Issue 28, 16 p.
- Parker, R. B. (Ed.), 1974, ERTS Issue: Univ. of Wyoming Contributions to Geology, Vol. 12, 110 p.
- Sales, J. K., 1983, Foreland deformation: a critique of cause: Am. Assoc. Petrol. Geol. Bull., Vol. 67, p. 1353-1354.
- Salomonson, V. V., P. L. Smith, Jr., A. B. Park, W. C. Webb, and T. J. Lynch, 1980, An overview of progress in the design and implementation of Landsat-D systems: IEEE Trans. Geoscience and Remote Sensing, Vol. GE-18, no. 2, p. 137-145.
- Soha, J. M., and A. A. Schwartz, 1978, Multispectral histogram normalization contrast enhancement: Proceedings of the Fifth Canadian Symposium on Remote Sensing, Victoria, p. 86-93.
- Stearns, D. W., 1975, Laramide basement deformation in the Bighorn Basin - the controlling factor for structures in the layered rocks: Wyoming Geol. Assoc., 27th Ann. Field Conf. Guide Book, p. 149-158.
- Stone, D. L., 1984, The Rattlesnake Mountain, Wyoming debate: A review and critique of models: The Mountain Geologist, Vol. 21, p. 37-46.
- Stone, W. D., 1972, Stratigraphy and exploration of the Lower Cretaceous Muddy Formation northern Powder River Basin, Wyoming and Montana: The Mountain Geologist, Vol. 9, p. 355-378.
- Thaden, R. E., 1980a, Geologic map of the Guffy Peak Quadrangle, showing chromolithofacies in the Wind River Formation, Fremont and Hot Springs Counties, Wyoming: U. S. Geol. Survey Geologic Quadrangle Map, GQ-1527.

Thaden, R. E., 1980b, Geologic map of the Picard Ranch Quadrangle, showing Chromolithofacies and coal beds in the Wind River Formation, Fremont County, Wyoming: U. S. Geol. Survey Geologic Quadrangle Map, GQ-1539.

Townshend, J. R. G., J. R. Gaylor, J. R. Hardy, M. J. Jackson, and J. R. Baker, 1983, Preliminary analysis of Landsat-4 Thematic Mapper products: Intl. Journal of Remote Sensing, Vol. 4, no. 4, p. 817-828.

Woodward, T. C., 1955, Geology of Deadman Butte area, Natrona County, Wyoming: Univ. Texas, Phd. Thesis.

Woodward, T. C., 1957, Geology of Deadman Butte area, Natrona County, Wyoming: Am. Assoc. Petrol. Geol. Bull., Vol. 41, p. 212-262.

## VIII. APPENDIX: PUBLICATIONS AND PRESENTATIONS

- Abrams, M. J., 1984, Landsat-4 Thematic Mapper and Thematic Mapper Simulator Data for a porphyry copper deposit: Photogrammetric Engineering and Remote Sensing, Vol. 50, p. 1171-1174.
- Abrams, M. J., A. B. Kahle, A. R. Gillespie, J. E. Conel, and Harold R. Lang, 1983, Geologic utility of Landsat-4 TM data: Presented by M. J. Abrams at the Landsat-4 Scientific Characterization Early Results Symposium at Goddard Space Flight Center, February 22-24.
- Conel, J. E., H. R. Lang., and E. D. Paylor, 1984, Preliminary atmospheric calibration and reflectance sensitivity studies on satellite and aircraft scanner data: Submitted for publication to the Proceedings of the Science Radiation and Atmospheric Effects Characterization (SRAEC) Fundamental Research Working Group, Fort Collins, Colorado, January.
- Conel, J. E., H. R. Lang, E. D. Paylor, and R. E. Alley, 1985, Preliminary spectral and geologic analysis of Landsat-4 Thematic Mapper data, Wind River Basin Area, Wyoming: IEEE Transactions on Geoscience and Remote Sensing, Vol. GE-23, no. 4, p. 562-573.
- Evans, D. and H. Lang, 1984, Techniques for multisensor image analysis: Invited Paper, ERIM, Paris, France.
- Kahle, A. B., and M. J. Abrams, 1983, Early Landsat-4 Thematic Mapper results in the Western United States: Presented by A. B. Kahle at the 4th Geosat Workshop, Remote Sensing Frontiers, at Flagstaff, Arizona, June 12-13.
- Lang, H. R., 1983, The Geologic Utility of Landsat-4 TM data: a comparison with other sensors: Presented by H. R. Lang at the Fall Convention of American Society of Photogrammetry, September 22, Salt Lake City, Utah.
- Lang, H. R., 1984, Recent advances in multispectral remote sensing: applications to Geology and Oil and Gas Exploration, American Chemical Society Division of Geochemistry, 187th ACS National Meeting, St. Louis, Missouri, GEOC 41.
- Lang, H. R., J. E. Conel, and E. D. Paylor, 1983, Preliminary geologic/spectral analysis of Landsat-4 Thematic Mapper data, Wind River/Bighorn Basin area, Wyoming: Presented by H. Lang at the Third Landsat-4 Workshop, December 6-7, GSFC, Greenbelt, MD.
- Lang, H. R., E. D. Paylor, and J. E. Conel, 1984, Spectral stratigraphy: A new tool for correlation and facies analysis, Permian-Upper Cretaceous, Casper arch area, Wyoming: Presented by H. R. Lang at the annual GSA Meeting, Reno, Nevada, GSA Abstracts with Programs, Vol. 16, no. 6, p. 568.
- Paylor, E. D., Lang, H. R., Abrams, M. J., Conel, J. E., and Kahle, A. B., 1985, Geologic evaluation of Landsat-4 Thematic Mapper data: Presented by E. Paylor at the LIDQA Final Symposium Special Session at the ACSM-ASP Fall Convention, September 8-13, Indianapolis, Indiana.

Paylor, E. D., H. R. Lang, and J. E. Conel, 1983, Preliminary spectral/stratigraphic analysis of Landsat-4 Thematic Mapper data, Wind River/Bighorn Basin area, Wyoming: Presented by E. Paylor at the Pecora VIII Symposium, October 4-7, p. 76.

Paylor, E. D., H. R. Lang, and J. E. Conel, 1984, Preliminary structural analysis of the Thermopolis anticline, Bighorn Basin, Wyoming: Presented at the Annual GSA Meeting, Reno, Nevada, AGSA Abstracts with Programs, Vol. 16, no. 664, p. 620.

Geographical distribution 31

52. Key Role, Successes & Failures  
of Psychotherapy and Rehabilitation

• 1901.18 von sich in Heidelberg. 18 (habe sich in) Heidelberg eingezogen. 19

## TECHNICAL REPORT STANDARD TITLE PAGE

1. Report No.	2. Government Accession No.	3. Recipient's Catalog No.
4. Title and Subtitle  Performance Evaluation and Geologic Utility of Landsat-4 Thematic Mapper Data		5. Report Date October 15, 1985
		6. Performing Organization Code
7. Author(s) Earnest D. Paylor, Michael J. Abrams, James E. Conel, Anne B. Kahle, Harold R. Lang, Jay B. Parrish		8. Performing Organization Report No. JPL Publication 85-66
9. Performing Organization Name and Address  JET PROPULSION LABORATORY California Institute of Technology 4800 Oak Grove Drive Pasadena, California 91109		10. Work Unit No.
		11. Contract or Grant No. NAS7-918
		13. Type of Report and Period Covered JPL Publication
12. Sponsoring Agency Name and Address  NATIONAL AERONAUTICS AND SPACE ADMINISTRATION Washington, D.C. 20546		14. Sponsoring Agency Code
15. Supplementary Notes		
16. Abstract This study was part of a continuing program at JPL for the development of remote sensing for geologic applications. The overall objective of the project was to evaluate Landat-4 Thematic Mapper (TM) data in the context of geologic applications. This involved a quantitative assessment of the data quality including the spatial and spectral characteristics realized by the instrument. Three test sites were selected for the study: 1) Silver Bell, Arizona; 2) Death Valley, California; and, 3) Wind River/Bighorn Basin area, Wyoming. Results of the study demonstrate that the TM sensor is a significant improvement compared to other satellite remote sensing systems. Conclusions include:  1. Artificial and natural targets can be used to atmospherically calibrate TM data and investigate scanner radiometry, atmospheric parameters, and construction of atmospheric Modulation Transfer Functions (MTF's). 2. No significant radiometric degradation occurs in TM data as a result of SCRUNGE processing; however, the data exhibit narrow digital number (DN) distributions suggesting that the configuration of the instrument is not optimal for earth science applications. 3. Increased spatial resolution, 1:24,000 enlargement capability, and good geometric fidelity of TM data allow accurate photogeologic/geomorphic mapping, including relative age dating of alluvial fans, measurement of structural and bedding attitudes, and construction of such things as structural cross sections and stratigraphic columns. 4. TM bands 5 and 7 are particularly useful for geologic applications because they span a region of the spectrum not previously sampled by multispectral scanner data and are important for characterizing clay and carbonate materials. This also allows the separation of iron-bearing and hydroxyl-bearing alteration zones associated with base and precious metal deposits.		
17. Key Words (Selected by Author(s))  Geology and Mineralogy  LANDSAT Project		18. Distribution Statement  Unclassified/Unlimited
19. Security Classif. (of this report)  Unclassified	20. Security Classif. (of this page)  Unclassified	21. No. of Pages  22. Price